

Cooperative Control of Bimanual Continuum Robots for Automated Knot-Tying in Robot-Assisted Surgical Suturing

Enoch Quaioco^{1*}, Ayman Nada², Hiroyuki Ishii³, Haitham El-Hussieny⁴

^{1,2,4} Department of Mechatronics and Robotics Engineering, Egypt-Japan University of Science and Technology, New Borg El-Arab, Alexandria, Egypt

³ Faculty of Science and Engineering, Waseda University, Shinjuku-ku, Tokyo, Japan

Email: ¹ enoch.quaioco@ejust.edu.eg, ² ayman.nada@ejust.edu.eg,

³ hiro.ishii@waseda.jp, ⁴ haitham.elhussieny@ejust.edu.eg

*Corresponding Author

Abstract—Knot-tying, a crucial yet intricate surgical task, remains a challenge in Robot-assisted Minimally Invasive Surgery (RAMIS) performed under teleoperation. While existing studies on automated knot-tying mostly focus on rigid-link robots, whose dexterity, adaptability, and inherent safety in RAMIS are outperformed by continuum robots, this research takes a novel approach by developing a unique cooperative control scheme for bimanual continuum robots, specifically designed for automated knot-tying tasks in RAMIS. We meticulously plan two effective knot-tying trajectory scenarios and develop the cooperative control scheme for the bimanual continuum robots, leveraging the well-known Jacobian transpose kinematic algorithms to ensure their precise and collaborative knot-tying trajectory tracking performance. The control scheme incorporates a switching mechanism to guarantee the robots' collaboration and synchronous operation during the knot-tying trajectory tracking process. The effectiveness of our cooperative control scheme is illustrated through simulation studies using MATLAB/Simulink in terms of trajectory tracking performance. Meanwhile, ten Monte Carlo simulations are conducted to analyze the system's robustness against pulse disturbances that could occur in surgical settings. All ten simulations returned similar error values despite the increasing disturbance levels applied. The results not only demonstrate the seamless collaboration and synchronous operation of the bimanual continuum robots in precisely tracking the pre-planned knot-tying trajectories with errors less than 0.0017 m but also highlight the stability, effective tuning and robustness of our cooperative control system against pulse disturbances. This study demonstrates precision, robustness, and autonomy in bimanual continuum robotic knot-tying in RAMIS, promising safe robot-patient interaction and reduced surgeon workload and surgery time.

Keywords—Continuum Robots; Automated Suture Knot-Tying; Surgical Suturing; Robot-Assisted Minimally Invasive Surgery; Trajectory Planning; Kinematic Modeling; Cooperative Control.

I. INTRODUCTION

The field of surgical robotics has experienced remarkable growth in recent years, leading to transformative changes

in healthcare practices. This evolution has been particularly pronounced in the realm of robot-assisted minimally invasive surgery (RAMIS), where surgeons are now equipped with enhanced control, precision, dexterity, and improved visual capabilities. These advancements translate into substantial patient benefits, including minimized trauma, reduced infection risks, and expedited recovery times, significantly outperforming traditional laparoscopic surgery methods [1]–[7].

Despite these advancements, certain surgical procedures are complex in RAMIS. Particularly in RAMIS suturing procedures, knot-tying remains intricate, tedious, and time-intensive. The challenges associated with knot-tying in RAMIS are exacerbated by the unstructured and limited surgical workspace, which restricts dexterity [8],[9]. Furthermore, the nonlinear deformations of sutures and suboptimal tensioning often result in sudden suture slippages, entanglements, or interferences with dual robot grippers within the limited workspace. These issues necessitate meticulous suture manipulation, precise tension control, and strategic motion planning. Effective coordination and control of two or more robot grippers are essential to comply with the spatial constraints of the surgical environment [8],[9].

The performance of RAMIS procedures, including knot-tying, is mostly based on teleoperation control by surgeons [10]–[13]. This presents a notable challenge due to limited haptic feedback in commercial teleoperated surgical systems despite the various proposed solutions [14]–[16]. Surgeons are often required to operate under non-intuitive vision systems, which can induce considerable cognitive strain. This aspect not only contributes to the inefficiency of surgical procedures but also extends their duration [9],[17]. Consequently, an emerging and pressing need exists to investigate and develop automated solutions within the RAMIS framework. The integration of automation aims to mitigate these challenges, thereby enhancing



surgical efficiency and reducing the cognitive load on surgeons [9],[17]–[19].

The shift towards automation in surgical robotics is a technological advancement and a fundamental reimagining of surgical practices. It promises to streamline surgical procedures, reduce human error, and ultimately optimize patient outcomes. As the surgical robotics field continues to evolve, the focus on automating complex surgical tasks, particularly in the context of RAMIS, becomes increasingly paramount, gaining many contributions [20]–[27]. This development trajectory signifies a critical leap in modernizing surgical methodologies and improving healthcare delivery.

Several innovative techniques have been proposed to address the challenges of automating the suture knot-tying task in RAMIS. For instance, deep-learning models [28] and calibrated stereo camera systems [29] have been introduced to automate the three-dimensional (3-D) tip position estimation or detection of the suture thread in order to eliminate the need for manual suture selection by surgeons during the knot-tying process. Building upon this, [30] extended the concept by showcasing a stereo vision-guided automatic suture grasping to facilitate autonomous knot-tying procedures. Further contributions in this domain include the introduction of the vision-guidance concept to automate knot-tying with an in-house robot vision system, where real-time monitoring of the two robot grippers was achieved through visual images [31]. These approaches represent a significant step in integrating advanced vision systems with autonomous robotic knot-tying control.

Whereas [31] focused on automating the suture looping subtask of knot-tying by proposing a dynamic (“rolling-arc”) suture looping trajectory planning approach, [32] introduced a task pose planner to automate the suture looping subtask of the knot-tying procedure using pre-planned spiral looping trajectories. The task pose was obtained through linear programming-based position optimization and brute force iterative orientation search.

Although many laparoscopic knot-tying techniques are available [33]–[35], their automated performance in RAMIS can be difficult. The dynamic rolling-arc and spiral looping techniques of the suture mentioned in [31],[32] are particularly suitable for automation due to their effectiveness in maintaining constant suture tension throughout the looping process to manage the nonlinear deformations and sudden slippages of the suture.

Despite these advancements, a thorough review of the literature reveals that most of the existing knot-tying techniques in RAMIS are grounded in rigid-link robotic principles. Because of the limited, confined, cluttered, and unstructured surgical workspaces that characterize RAMIS, the constraints of rigid-link robots, including their limited sizes and degrees of freedom (DoF), non-compliance, reduced adaptability, and difficulty in interacting with delicate tissues and organs in confined surgical

environments pose significant challenges, particularly in safe robot-patient interaction and optimal performance [36]–[38]. Addressing these limitations necessitates a shift towards more flexible, compliant, and adaptable robotic systems that can exhibit high levels of dexterity, reachability, and motion control accuracy in the confined surgical workspace.

Against the backdrop of rigid-link robots, continuum robots have emerged as a groundbreaking technological advancement in many fields of robotics. Their applications extend to industrial manipulation tasks [39], explorations in the deep-sea [40]–[42], navigation in cluttered environments [43], and medical (surgical) interventions [44].

Characterized by their exceptional dexterity and compliance, infinite degree of freedom (DoF), and small, continuous structures, continuum robots offer significant potential for enhancing the safety and effectiveness of RAMIS procedures as they can adapt to and safely interact with delicate, unstructured, and confined surgical environments [37],[38],[45].

However, continuum robots undergo continuous bending or structural deformations to generate their motions, thus presenting their modeling and control difficulties. This has led several research studies to focus on the design and modeling approaches of continuum robots [46]–[55], their actuation principles and technologies [56]–[60], learning-based and model-based control strategies [61]–[70], and their sensing techniques [71]–[73] to improve optimal performance.

Despite the progress achieved in developing and deploying continuum robotic systems for surgical procedures, their collaborative control for certain complex tasks in RAMIS, such as suture knot-tying, is predominantly confined to the surgeon’s direct command through teleoperation [12],[74].

Therefore, considering surgeons’ tedium, deprived sense of feeling, and high cognitive burden in teleoperating RAMIS procedures, there is a pressing need for continuum robots’ autonomous execution of this tedious and time-intensive knot-tying task within RAMIS. This could improve repeatability, motion quality, adaptability, and safe robot-patient interaction while alleviating the high cognitive workloads on surgeons and potentially reducing overall surgery time [9],[17]–[19].

Some researchers have focused on continuum robots’ autonomous navigation motion planning techniques for intraluminal procedures and endovascular interventions based on the node, sampling, optimization, and learning approaches, as extensively discussed by [75]. Further notable developments in continuum robots’ autonomous task execution include their fully automated control approach for steerable guidewire navigation within vessels using fluoroscopic image-based 3-D environment reconstruction [76] and the force-perceptive, safe, semi-autonomous navigation of the continuum robotic ValveTech platform prior to aortic valve implantation [77].

While [75]–[77] and several other studies have explored the

autonomous control of continuum robots in specific surgical scenarios, the literature study reveals a notable gap in research on autonomous knot-tying motions generated and controlled by continuum robots. Bridging this gap could significantly contribute to the advancement of autonomous surgical capabilities in continuum robotic systems.

This paper contributes primarily to developing a novel kinematic-based cooperative control strategy specifically designed for bimanual continuum robots. This strategy is focused on ensuring seamless collaboration and synchronous operation of the robots, facilitating the precise and automatic execution of pre-planned knot-tying trajectories. Emphasis is placed on achieving enhanced tracking performance and increased robustness against disturbances, as these are critical factors in robot-assisted surgical applications.

The research draws inspiration from the spiral and rolling-arc looping knot-tying techniques, as detailed in [31],[32], to plan and implement two distinct knot-tying reference trajectories using MATLAB. These trajectories are carefully designed to leverage the unique capabilities of the bimanual continuum robots through their collaboration and coordination in performing complex surgical knot-tying tasks while avoiding sudden suture slippages and collision between the robots' tip grippers.

Further, the proposed control system has been implemented and tested in MATLAB/Simulink, simulating the environment and conditions typical in surgical settings. This implementation is based on the kinematics of two-section bimanual continuum robots specifically tailored for this application. The consideration for two-section bimanual continuum robots instead of single-section robots has the advantage of sufficient DoF and flexibility for the surgical knot-tying application.

In this research, the dynamics of the continuum robots are intentionally omitted in the modeling and control process. This decision is substantiated by the inherent slenderness of continuum robot arms and the relatively slow movements that characterize surgical procedures. By focusing on kinematics, the control strategy efficiently addresses the primary challenges of automating surgical knot-tying using continuum robots, offering a significant advancement in the surgical robotics field.

The remainder of this paper is laid out as follows. In Section II, we present the kinematic modeling of the proposed two-section bimanual continuum robots. In Section III, we plan the automated knot-tying trajectories of the bimanual continuum robots, whereas Section IV presents the implementation of the proposed cooperative control scheme to achieve the automated knot-tying task. In Section V, we present discussions of the results obtained from the simulation experiments undertaken to evaluate the effectiveness of the proposed control system developed for bimanual continuum robots' surgical knot-tying applications. Finally, we present the conclusion and future works in Section VI.

II. KINEMATICS MODELING

To control the proposed two-section bimanual continuum robots to follow pre-planned knot-tying trajectories, the kinematics model defining each robot's tip positions relative to the base is key. Fig. 1 illustrates the structure of a two-section continuum robot. Each section i (where $i = 1, 2, 3, \dots, N$) of a multi-section continuum robot can be described as an arc of a circle in space with configuration parameters s_i , κ_i , and ϕ_i , which represent the arc length, curvature, and direction of curvature (rotation in xy plane), respectively. In order to avoid the singular configuration of continuum robots, $\kappa_i \neq 0$.

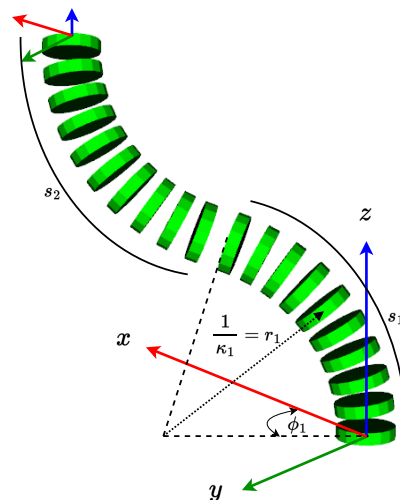


Fig. 1. Illustration of the structure of a two-section continuum robot arm. The shape or configuration parameters s_1 , κ_1 , ϕ_1 , and r_1 represent the arc length, curvature, direction of curvature (rotation in xy plane), and radius of curvature of the proximal section of the robot arm, respectively. s_2 represents the arc length of the distal section of the robot arm.

A. Modeling Assumptions

The well-known constant curvature kinematics modeling approach [55],[68] is adopted in this research with a focus on the robot-independent mapping between the task space parameters and the configuration space parameters of the robots. Thus, we neglect the robot-specific mapping between the configuration space parameters and the actuator inputs, such as the tendon lengths, in the kinematic modeling process. This could inaccurately represent continuum robots' complex behaviors in realistic situations where variable actuator inputs are required to drive the physical robots. However, it simplifies and generalizes the kinematic control and simulation problem to any continuum robot type based on the constant curvature model.

In line with the constant curvature approach, we also assume that the proposed two-section bimanual continuum robots are non-extensible; that is, the arc length s_i of each section i of the robots is constant or fixed and does not vary during the robots' tip motion generation. Although this assumption

aligns with the constant curvature approach, it could limit the extensibility, reachability, and dexterity of continuum robots, especially single-section continuum robots, in performing complex tasks and avoiding obstacles in the workspace. However, multi-section continuum robot models, which we adopt in this research, could significantly improve the reachability, dexterity or flexibility of continuum robots in performing complex tasks, such as suture knot-tying in constrained environments.

It is worth discussing that the assumption of constant curvature along continuum robots' structures may result in inaccurate prediction of complex trajectories, particularly motions involving sharp turns. Therefore, advanced modeling approaches, such as finite element-based methods [49] and variable curvature models [51],[52],[78] that consider the sudden curvature changes of continuum robots could be explored in future studies to mitigate these limitations. However, despite the limitations mentioned, the constant curvature kinematics modeling approach can prove effective in assessing the feasibility and potential effectiveness of the proposed cooperative control approach.

B. Forward Kinematics

The forward kinematics of each of the proposed two-section bimanual continuum robots A and B can be expressed based on the coordinate homogeneous transformation matrix system. The homogeneous transformation matrix defines the pose (position and orientation) of the continuum robot's tip coordinate frame relative to the base coordinate frame. Thus, for any multi-section continuum robot (with sections $i = 1, 2, 3, \dots, N$), the homogeneous transformation matrix ${}^{i-1}\mathbf{T}_i \in \mathbb{R}^{4 \times 4}$ defining the pose of the tip coordinate frame $\{i\}$ of each section i of the robot relative to the base coordinate frame $\{i-1\}$ of the section i can be stated as follows [68],

$${}^{i-1}\mathbf{T}_i = \begin{bmatrix} {}^{i-1}\mathbf{R}_i & {}^{i-1}\mathbf{X}_i \\ 0 & 1 \end{bmatrix} \in \mathbb{R}^{4 \times 4} \quad (1)$$

where ${}^{i-1}\mathbf{R}_i \in \mathbb{R}^{3 \times 3}$ and ${}^{i-1}\mathbf{X}_i \in \mathbb{R}^{3 \times 1}$ represent the rotation matrix and the translation (position) vector, respectively, which are stated as follows,

$${}^{i-1}\mathbf{R}_i = \begin{bmatrix} \cos^2 \phi_i (\cos \kappa_i s_i - 1) + 1 & & & \\ \sin \phi_i \cos \phi_i (\cos \kappa_i s_i - 1) & & & \\ \cos \phi_i \sin \kappa_i s_i & & & \\ \sin \phi_i \cos \phi_i (\cos \kappa_i s_i - 1) & -\cos \phi_i \sin \kappa_i s_i & & \\ \cos^2 \phi_i (1 - \cos \kappa_i s_i) + \cos \kappa_i s_i & -\sin \phi_i \sin \kappa_i s_i & & \\ \sin \phi_i \sin \kappa_i s_i & \cos \kappa_i s_i & & \end{bmatrix} \quad (2)$$

$${}^{i-1}\mathbf{X}_i = \begin{bmatrix} \cos \phi_i (\cos \kappa_i s_i - 1) / \kappa_i \\ \sin \phi_i (\cos \kappa_i s_i - 1) / \kappa_i \\ \sin(\kappa_i s_i) / \kappa_i \end{bmatrix} \in \mathbb{R}^{3 \times 1} \quad (3)$$

In (2), the first, second, and third columns of ${}^{i-1}\mathbf{R}_i \in \mathbb{R}^{3 \times 3}$

define the x , y , and z orientations of the tip coordinate frame $\{i\}$ of each section i of the robot relative to the base coordinate frame $\{i-1\}$ of the section i , respectively. The position vector ${}^{i-1}\mathbf{X}_i \in \mathbb{R}^{3 \times 1}$ given by (3) defines the positions of the tip coordinate frame $\{i\}$ of each section i of the robot relative to the base coordinate frame $\{i-1\}$ of the section i .

For the multi-section continuum robot (with sections $i = 1, 2, 3, \dots, N$), the homogeneous transformation matrix ${}^0\mathbf{T}_N$ defining the pose of the robot's tip or end-effector coordinate frame $\{N\}$ relative to the base coordinate frame $\{0\}$ can be computed as follows,

$${}^0\mathbf{T}_N = \prod_{i=1}^N {}^{i-1}\mathbf{T}_i \in \mathbb{R}^{4 \times 4} \quad (4)$$

Therefore, from (4), we can compute the homogeneous transformation matrix ${}^0\mathbf{T}_2$ defining the tip or end-effector pose relative to the base of each of the proposed two-section bimanual continuum robots A and B as follows,

$${}^0\mathbf{T}_2 = \prod_{i=1}^2 {}^{i-1}\mathbf{T}_i = \begin{bmatrix} {}^0\mathbf{R}_2 & {}^0\mathbf{X}_2 \\ 0 & 1 \end{bmatrix} \in \mathbb{R}^{4 \times 4} \quad (5)$$

where ${}^0\mathbf{R}_2 \in \mathbb{R}^{3 \times 3}$ represents the rotation matrix defining the xyz orientations of each robot's tip coordinate frames relative to the base and ${}^0\mathbf{X}_2 \in \mathbb{R}^{3 \times 1}$ represents the position vector defining each robot's tip positions relative to the base. In (5), each of the matrix terms for ${}^0\mathbf{R}_2 \in \mathbb{R}^{3 \times 3}$ and ${}^0\mathbf{X}_2 \in \mathbb{R}^{3 \times 1}$ is obtained as a multivariate function of the configuration parameters $\mathbf{q} = (s_1, \kappa_1, \phi_1, s_2, \kappa_2, \phi_2)$ of both sections of each continuum robot. ${}^0\mathbf{X}_2 \in \mathbb{R}^{3 \times 1}$ expresses the forward kinematics of each two-section continuum robot in terms of the nonlinear relationship between the task space (tip) parameters (x, y, z) and the configuration space parameters \mathbf{q} .

Thus, the forward kinematics models ${}^0\mathbf{X}_{2A}$ and ${}^0\mathbf{X}_{2B}$ for the proposed two-section bimanual continuum robots A and B can be written in the following nonlinear forms, respectively,

$${}^0\mathbf{X}_{2A} = \begin{bmatrix} x_A \\ y_A \\ z_A \end{bmatrix} = \begin{bmatrix} \mathbf{f}_x(\mathbf{q}_A) \\ \mathbf{f}_y(\mathbf{q}_A) \\ \mathbf{f}_z(\mathbf{q}_A) \end{bmatrix} \in \mathbb{R}^{3 \times 1} \quad (6)$$

$${}^0\mathbf{X}_{2B} = \begin{bmatrix} x_B \\ y_B \\ z_B \end{bmatrix} = \begin{bmatrix} \mathbf{f}_x(\mathbf{q}_B) \\ \mathbf{f}_y(\mathbf{q}_B) \\ \mathbf{f}_z(\mathbf{q}_B) \end{bmatrix} \in \mathbb{R}^{3 \times 1} \quad (7)$$

Note that the subscripts A and B only specify the parameters of robot A and robot B , respectively.

C. Differential Kinematics

The main point of kinematic control of the bimanual continuum robots A and B is the solutions to their inverse kinematics

problems in (6) and (7) in order to determine the configuration parameters \mathbf{q}_A and \mathbf{q}_B that correspond to their desired states (tip positions) in the task space. However, finding these solutions can be challenging due to the nonlinearity of (6) and (7) mentioned earlier. Therefore, we resort to differential kinematics as an effective numerical approach to solve the inverse kinematics control problem [79]. The differential mapping between the task space (tip) velocities ${}^0\dot{\mathbf{X}}_{2_A} \in \mathbb{R}^{3 \times 1}$ and ${}^0\dot{\mathbf{X}}_{2_B} \in \mathbb{R}^{3 \times 1}$ and the configuration space velocities $\dot{\mathbf{q}}_A$ and $\dot{\mathbf{q}}_B$ of the bimanual continuum robots A and B can be stated as follows, respectively,

$${}^0\dot{\mathbf{X}}_{2_A} = \mathbf{J}_{\mathbf{q}_A} \times \dot{\mathbf{q}}_A \in \mathbb{R}^{3 \times 1} \quad (8)$$

$${}^0\dot{\mathbf{X}}_{2_B} = \mathbf{J}_{\mathbf{q}_B} \times \dot{\mathbf{q}}_B \in \mathbb{R}^{3 \times 1} \quad (9)$$

The advantage of the differential mappings in (8) and (9) over (6) and (7) lies in the linear relationship between the derivatives of the continuum robots' states (tip positions) ${}^0\mathbf{X}_{2_A}$ and ${}^0\mathbf{X}_{2_B}$ in the task space and their states \mathbf{q}_A and \mathbf{q}_B in the configuration space, which is given by $\mathbf{J}_{\mathbf{q}_A}$ and $\mathbf{J}_{\mathbf{q}_B}$ as follows, respectively,

$$\mathbf{J}_{\mathbf{q}_A} = \frac{\partial {}^0\mathbf{X}_{2_A}}{\partial \mathbf{q}_A} = \frac{\partial [x_A, y_A, z_A]^T}{\partial (\kappa_1, \phi_1, \kappa_2, \phi_2)_A} \in \mathbb{R}^{3 \times 4} \quad (10)$$

$$\mathbf{J}_{\mathbf{q}_B} = \frac{\partial {}^0\mathbf{X}_{2_B}}{\partial \mathbf{q}_B} = \frac{\partial [x_B, y_B, z_B]^T}{\partial (\kappa_1, \phi_1, \kappa_2, \phi_2)_B} \in \mathbb{R}^{3 \times 4} \quad (11)$$

where $\mathbf{J}_{\mathbf{q}_A} \in \mathbb{R}^{3 \times 4}$ and $\mathbf{J}_{\mathbf{q}_B} \in \mathbb{R}^{3 \times 4}$ represent the analytical Jacobians, which facilitate the configuration space velocity control of the bimanual continuum robots A and B . Note that in (10) and (11), we have neglected the partial derivatives of the robots' states (tip positions) in the task space with respect to the arc length components of the configuration parameters. This is owing to the assumption of constant or fixed arc length parameters for the robots' sections during their tip motion generation, as mentioned earlier in Section II-A.

D. Jacobian Transpose Kinematic Algorithm

Since the computed analytical Jacobians from (10) and (11) are non-square matrices, finding solutions to the differential kinematics problems in (8) and (9) based on direct inversion of the Jacobians is not possible. Therefore, we resort to the well-known Jacobian transpose kinematic algorithm to solve the differential kinematic control problem for the bimanual continuum robots A and B as follows, respectively,

$$\dot{\mathbf{q}}_A = \mathbf{J}_{\mathbf{q}_A}^T \times (\mathbf{K}_A \times \mathbf{e}_A) \in \mathbb{R}^{4 \times 1} \quad (12)$$

$$\dot{\mathbf{q}}_B = \mathbf{J}_{\mathbf{q}_B}^T \times (\mathbf{K}_B \times \mathbf{e}_B) \in \mathbb{R}^{4 \times 1} \quad (13)$$

where $\mathbf{J}_{\mathbf{q}_A}^T \in \mathbb{R}^{4 \times 3}$ and $\mathbf{J}_{\mathbf{q}_B}^T \in \mathbb{R}^{4 \times 3}$ represent the transpose of the analytical Jacobians, whereas $(\mathbf{K}_A \times \mathbf{e}_A)$ and $(\mathbf{K}_B \times \mathbf{e}_B)$ are the feedback correction terms, which are introduced in order to eliminate any numerical drift that may occur in the solution. The computed configuration space velocities $\dot{\mathbf{q}}_A \in \mathbb{R}^{4 \times 1}$ and $\dot{\mathbf{q}}_B \in \mathbb{R}^{4 \times 1}$ from (12) and (13) can then be integrated over time to obtain the resulting configuration parameters $\mathbf{q}_A \in \mathbb{R}^{4 \times 1}$ and $\mathbf{q}_B \in \mathbb{R}^{4 \times 1}$ that correspond to the desired tip positions of the robots. $\mathbf{K}_A \in \mathbb{R}^{3 \times 3}$ and $\mathbf{K}_B \in \mathbb{R}^{3 \times 3}$ are the suitably selected positive definite gain matrices for proper tuning of the robots' controllers. $\mathbf{e}_A \in \mathbb{R}^{3 \times 1}$ and $\mathbf{e}_B \in \mathbb{R}^{3 \times 1}$ are the errors between the reference and the actual task space parameters of robots A and B , respectively. These errors can be computed as follows,

$$\mathbf{e}_A = \mathbf{X}_{A(r)} - \mathbf{X}_{A(a)} \in \mathbb{R}^{3 \times 1} \quad (14)$$

$$\mathbf{e}_B = \mathbf{X}_{B(r)} - \mathbf{X}_{B(a)} \in \mathbb{R}^{3 \times 1} \quad (15)$$

where $\mathbf{X}_{A(a)} = {}^0\mathbf{X}_{2_A} \in \mathbb{R}^{3 \times 1}$ and $\mathbf{X}_{B(a)} = {}^0\mathbf{X}_{2_B} \in \mathbb{R}^{3 \times 1}$ are the actual task space parameters representing the set of actual tip positions of robots A and B , respectively. $\mathbf{X}_{A(r)} \in \mathbb{R}^{3 \times 1}$ and $\mathbf{X}_{B(r)} \in \mathbb{R}^{3 \times 1}$ are the reference task space parameters representing the set of reference or desired tip positions of robots A and B , respectively.

In what follows in Section III, we illustrate the automated knot-tying trajectory planning and then present in Section IV the resulting cooperative control scheme implemented based on the Jacobian transpose kinematic algorithms to solve the kinematic control problem of the bimanual continuum robots for tracking the pre-planned knot-tying trajectories precisely.

Although our cooperative control approach focuses on the Jacobian transpose kinematic algorithm, which proves effective and guarantees limited tracking and null steady-state errors, the Jacobian pseudo-inverse kinematic algorithm could be directly applied to this research.

III. AUTOMATED KNOT-TYING TRAJECTORY PLANNING

Typically, in robotic surgical suturing, the knot-tying task follows the needle-driving procedure and involves the following sequence of processes. Initially, one robot gripper grasps a point of the suture "leading" section (i.e., the section of suture that exits the tissue with the needle after the needle-driving procedure) and winds suture loops around a second robot gripper. The second robot gripper then grasps the suture "tail" point (i.e., the other free end of the suture) and pulls it through the loops via a process called unlooping to create the knot.

In our automated knot-tying trajectory planning approach, we assume that the grasp points of the suture "leading" and "tail" sections are known to the system and can be selected under the surgeon's supervision. Also, the surgeon manually controls

the initial grasping and appropriate tensioning of the suture “leading” section. With the bimanual continuum robots at the desired initial states and one of the robot grippers holding the suture “leading” section in tension, we meticulously plan their collaborative, collision-free, and automatic execution of knot-tying trajectories. In what follows in Sections III-A and III-B, we illustrate two different scenarios of automated knot-tying trajectory planning for the bimanual continuum robots taking inspiration from the spiral looping and the rolling-arc looping techniques. These suture looping techniques are particularly suitable for automating the complex knot-tying task in RAMIS and effective in managing the nonlinear deformations and sudden slippages of the suture [31],[32].

A. Spiral Looping-based Knot-tying Trajectory Planning

We have provided three-dimensional (3-D) and two-dimensional (2-D) illustrations of the spiral looping-based knot-tying trajectory planning for the bimanual continuum robots *A* and *B* shown in Fig. 2 and Fig. 3, respectively. These illustrations provide a clear and comprehensive view of the knot-tying process, capturing the intricate suture looping, suture “tail” point grasping, and unlooping for knot forming.

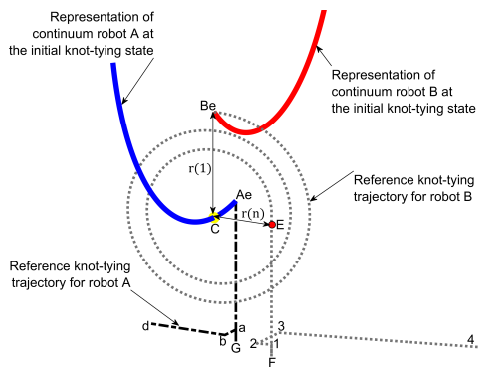


Fig. 2. 3-D illustration of the spiral looping-based knot-tying trajectory planning for the bimanual continuum robots *A* and *B*. The blue arc indicates the initial state of the continuum robot arm *A* at the start of knot-tying, with *Ae* indicating its tip position. The red arc indicates the initial state of the continuum robot arm *B* at the start of knot-tying, with *Be* indicating its tip position. Trajectory *Be-E* indicates robot *B*'s spiral looping trajectory around the point *C* of robot arm *A*, which begins at tip position *Be* with an initial radius $r(1)$ and ends at position *E* with a final radius $r(n)$. Trajectories *Ae-G*, *G-a*, *a-b*, *b-d* indicate the sequence of linear trajectories executed by robot *A* and *E-F*, *F-1*, *1-2*, *2-3*, *3-4* indicate the sequence of linear trajectories executed by robot *B* after the spiral looping for the suture “tail” point grasping from position *G* and lifting to position *a* by robot *A* and the simultaneous unlooping process by both robots *A* and *B* for knot forming and tightening.

1) *Suture Looping*: With bimanual continuum robots *A* and *B* at the desired initial states for knot-tying as illustrated in Fig. 2 and Fig. 3, robot *B* tip gripper *Be*, which initially holds the suture “leading” section in tension, begins to execute the spiral trajectory *Be-E* to wrap or loop the suture around the stationary robot *A*. The selected point *C* closer to the tip of robot arm *A* is where the suture loops are formed and is termed the looping point. As shown in Fig. 3, *e* is the small distance

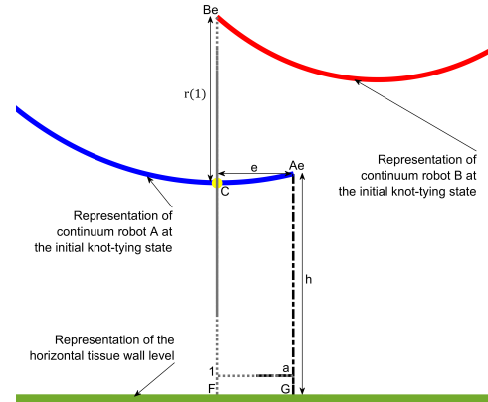


Fig. 3. 2-D illustration of the spiral looping-based knot-tying trajectory planning for the bimanual continuum robots *A* and *B*. Note that this figure complements Fig. 2 for clarity and visualization purposes. *h* indicates the suture “tail” point grasping distance from robot *A*'s tip point *Ae* (approximately point *C*) to the horizontal tissue wall. The point *C* closer to the tip of robot *A* indicates the looping point where the suture loops are formed around robot *A*. *e* indicates the small distance between the point *C* and the tip *Ae* of robot *A*. $r(1)$ indicates the initial spiral looping radius between robot *B*'s tip *Be* and the point *C* of robot arm *A* such that $r(1) < h$.

from the tip of robot *A* to the looping point *C*. Hence, with the coordinates of the looping point defined as $C = (C_x, C_y, C_z)$, robot *B*'s spiral looping trajectory *Be-E* about this point *C* of the robot arm *A* can be described as follows,

$$\begin{bmatrix} x_m \\ y_m \\ z_m \end{bmatrix}_{\text{spiral}} = \begin{bmatrix} C_x \\ C_y - r(m) \times \cos \theta(m) \\ C_z - r(m) \times \sin \theta(m) \end{bmatrix} \quad (16)$$

$$r(m) = r(m-1) - \frac{r(1) - r(n)}{n} \quad (17)$$

$$r(1) = r(n) + (\pi \times d_A \times L) \quad (18)$$

where (16) can be used to compute the set of vector points $[x_m, y_m, z_m]_{\text{spiral}}^T$ representing robot *B*'s tip coordinate positions along the spiral looping trajectory *Be-E* (see Fig. 2). The angle θ ranges from 0 to $2\pi \times L$, where *L* is the number of suture windings to form loops around robot arm *A*. The dimensionless parameter $m = 1, 2, 3, \dots, n$ defines or parameterizes the spiral looping trajectory points. (17) can be used to compute the radius $r(m)$ at each point of the spiral looping trajectory.

In (17) and (18), $r(1)$ is the initial spiral looping radius between robot *B*'s tip gripper *Be* and the looping point *C* of robot arm *A* (see Fig. 3). $r(1)$ must be less than the vertical distance *h* between the horizontal tissue wall and robot *A*'s tip point *Ae* (or point *C* approximately). The condition $r(1) < h$ is an important and safe condition for keeping robot *B*'s tip gripper from scratching the tissue wall during the suture looping process. $r(1)$ also indicates the length of the suture “leading” section initially held in tension by robot *B* that will be used during the looping process. Again in (17) and (18), $r(n)$ is the final spiral looping radius, which also indicates the remaining length of the suture “leading” section kept in tension between

the point C of the stationary robot arm A and robot B 's tip gripper at the end point E of the spiral looping trajectory (see Fig. 2). This final spiral looping radius $r(n)$ is a critical parameter that is appropriately defined (selected) during the initial trajectory planning because it serves as a clearance to ensure collision-free between the bimanual continuum robots A and B at the end of the spiral looping trajectory. Therefore, with $r(n)$ appropriately defined, (18) can be used to properly determine the initial looping radius $r(1)$ to satisfy the limited workspace conditions and ensure a collision-free suture looping process. In (18), d_A is the miniature diameter of robot arm A , whereas L representing the number of suture windings to form loops around robot arm A is chosen to be 2.25.

In (17), the term $\frac{r(1) - r(n)}{n}$ represents the continuous or constant rate of change (reduction) of the radius along the spiral looping trajectory, i.e., from the initial radius $r(1)$ to the smaller final radius $r(n)$. This is equal to the rate of change or reduction of the length of the suture "leading" section being looped around the stationary robot arm A . As a result of this, the appropriate suture tension can be kept constant throughout the entire spiral looping process to prevent the over-tensioning of the suture to avoid any breakage and the under-tensioning of the suture to avoid any sudden slippages and tangling.

2) *Suture Tail Point Grasping*: At the end of the suture looping process, robot A is then required to move downwards from its stationary tip position Ae along trajectory $Ae-G$ to grasp the predefined (selected) suture "tail" point G from the tissue wall (see Fig. 2 and Fig. 3). However, this downward movement for suture "tail" point grasping can not be achieved by robot A in isolation from robot B since both robots are adjoined by the remaining suture length $r(n)$ at the end of the suture looping process. Therefore, both robots A and B move downward simultaneously (synchronously) and along the parallel trajectories $Ae-G$ and $E-F$, respectively (see Fig. 2). With the selected suture "tail" point G grasped by robot A , both robots A and B then continue their synchronous and parallel movement upwards along trajectories $G-a$ and $F-1$, respectively, lifting the grasped suture "tail" to keep safety clearance off the tissue wall.

This synchronous and parallel movement by both robots A and B along the trajectories $(Ae-G, G-a)$ and $(E-F, F-1)$, respectively, for suture "tail" point grasping and lifting maintains the constant tension of the remaining suture length $r(n)$ adjoining the robots. This prevents the over-tensioning and breakage of the suture. Most importantly, keeping the appropriate initial suture tension constant during this process prevents the under-tensioning of the suture, which could cause premature unlooping and slip-off of the suture loops formed around robot A .

3) *Suture Unlooping for Knot Forming*: With robots A and B now at tip positions a and 1 respectively after the suture "tail"

point grasping and lifting process, robot A keeps stationary at position a while robot B moves a small distance closer towards the stationary robot A along trajectory 1-2 (see Fig. 2). This movement is important because it loosens the constant tension kept in the remaining suture length $r(n)$ that adjoins the robots. Thus, the suture loops formed around robot arm A become a bit loose to ease the unlooping process. During this process, robot A and robot B at tip positions a and 2 , respectively, begin to move simultaneously or synchronously along parallel but opposite trajectories $a-b$ and $2-3$, respectively (see Fig. 2). This synchronous and parallel but opposite movement by both robots A and B causes the suture loops formed around the robot arm A to slip off while effectively pulling the grasped suture "tail" section through to create a loose knot. Finally, robots A and B continue their synchronous, parallel, and opposite movement along trajectories $b-d$ and $3-4$, respectively, to tighten the knot created. This completes the first throw of knot-tying but may not necessarily produce a stable knot. Therefore, the entire knot-tying procedure described can be repeated for a second throw to ensure a more stable and reliable knot.

Hence, the sequence of linear trajectories $Ae-G, G-a, a-b, b-d$ executed by robot A and $E-F, F-1, 1-2, 2-3, 3-4$ executed by robot B during suture "tail" point grasping and lifting and unlooping for knot forming and tightening processes can be described as follows,

$$\begin{bmatrix} x_j \\ y_j \\ z_j \end{bmatrix}_{linear} = \begin{bmatrix} x_0 + (j \times t_x) \\ y_0 + (j \times t_y) \\ z_0 + (j \times t_z) \end{bmatrix} \quad (19)$$

where $[x_j, y_j, z_j]_{linear}^T$ is the set of the computed vector points representing the tip coordinate positions of robot A and robot B along their designed linear trajectory points, respectively. $[x_0, y_0, z_0]^T$ represents the starting vector points of the linear trajectories. The dimensionless parameter $j = 0, 1, 2, 3, \dots, n$ defines or parameterizes the linear trajectory points, whereas $[t_x, t_y, t_z]^T$ represents their direction ratios (orientations).

B. Rolling-arc Looping-based Knot-tying Trajectory Planning

Our meticulous rolling-arc looping-based knot-tying trajectory planning for the bimanual continuum robots A and B is showcased in the 3-D and 2-D illustrations in Fig. 4 and Fig. 5, respectively. These illustrations provide vivid demonstrations of the knot-tying process, capturing the intricate suture looping, suture "tail" point grasping, and unlooping for knot forming.

1) *Suture Looping*: The rolling-arc suture looping process is a meticulously sequenced operation that underscores the precision and coordination required in the field of surgical robotics. This delicate interplay between the bimanual continuum robots A and B , as illustrated in Fig. 4 and Fig. 5, is a testament to the intricacy and significance of our research. With bimanual

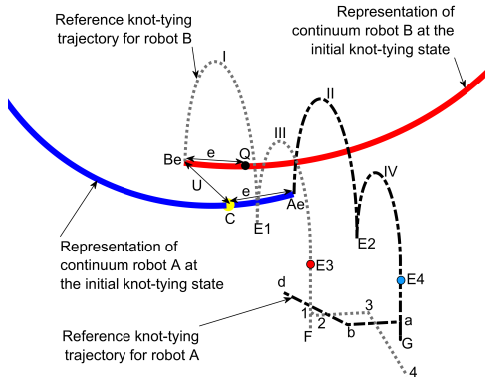


Fig. 4. 3-D illustration of the rolling-arc looping-based knot-tying trajectory planning for the bimanual continuum robots A and B. The blue arc indicates the initial state of the continuum robot arm A at the start of knot-tying, with Ae indicating its tip position. The red arc indicates the initial state of the continuum robot arm B at the start of knot-tying, with Be indicating its tip position. The point C closer to the tip of robot A indicates the looping point where the suture loops are formed around robot A. e indicates the small distance between the point C and the tip Ae of robot arm A and that between the point Q and the tip Be of robot arm B. Trajectories I and III indicate robot B’s rolling-arc looping trajectories from tip position Be to E1 and from E1 to E3, respectively. Trajectories II and IV indicate robot A’s rolling-arc looping trajectories from tip position Ae to E2 and from E2 to E4, respectively (see Fig. 2 for a clear 2-D visualization). Trajectories E4–G, G–a, a–b, b–d indicate the sequence of linear trajectories executed by robot A and E3–F, F–1, 1–2, 2–3, 3–4 indicate the sequence of linear trajectories executed by robot B after the rolling-arc looping for the suture “tail” point grasping from position G and lifting to position a by robot A and the simultaneous unlooping process by both robots A and B for knot forming and tightening.

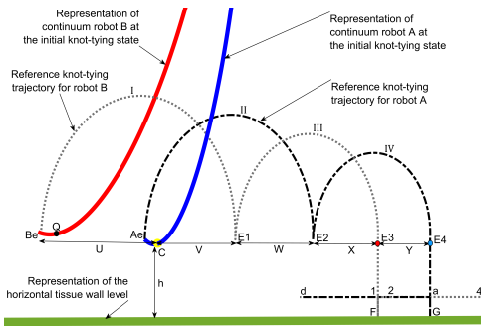


Fig. 5. 2-D illustration of the rolling-arc looping-based knot-tying trajectory planning for the bimanual continuum robots A and B. Note that this figure complements Fig. 2 for clarity and visualization purposes. U indicates the initial radius of robot B’s arc trajectory I between its tip Be and the looping point C of robot arm A (see Fig. 2 for a clear 3-D visualization). V serves as the final radius of robot B’s arc trajectory I and the initial radius of robot A’s arc trajectory II. W serves as the final radius of robot A’s arc trajectory II and the initial radius of robot B’s arc trajectory III. X serves as the final radius of robot B’s arc trajectory III and the initial radius of robot A’s arc trajectory IV. Y indicates the final radius of robot A’s arc trajectory IV. h indicates the suture “tail” point grasping distance from robot A’s tip point Ae (approximately point C) to the horizontal tissue wall.

continuum robots A and B at the desired initial states for knot-tying (see Fig. 4), the process begins with robot B tip gripper Be, which initially holds the suture “leading” section in tension, executing an arc trajectory I over the stationary robot arm A. This arc movement by robot B does not form a complete suture loop around robot arm A. While robot B is kept stationary at tip position E1 at the end of the arc trajectory I, robot A then moves from its initially stationary tip position Ae to execute

the arc trajectory II. This arc movement by robot A completes one full suture loop around its arm. With robot A now kept stationary at tip position E2 at the end of the arc trajectory II, robot B then moves from its stationary tip position E1 to execute the arc trajectory III to complete one-and-half suture looping around robot arm A. Finally, while robot B is kept stationary at tip position E3 at the end of the arc trajectory III, robot A then moves from its stationary tip position E2 to execute the arc trajectory IV, thereby completing two full suture loops around robot arm A as desired. At the end of the rolling-arc suture looping process, the bimanual continuum robots A and B are at tip positions E4 and E3, respectively (see Fig. 5).

As shown in Fig. 4, the selected point C closer to the tip of robot arm A is where the suture loops are formed and is termed as the looping point, whereas e is the small distance from the tip of robot A to the looping point C. Therefore, the center point coordinates of robot B’s arc trajectories I and III can be determined based on the coordinates of the looping point C of robot arm A when the robot A is stationary at the initial tip position Ae and tip position E2, respectively. Similarly, the center point coordinates of robot A’s arc trajectories II and IV can be determined based on the coordinates of the point Q of robot arm B when the robot B is stationary at tip position E1 and tip position E3, respectively (see Fig. 4 and Fig. 5). Each of the rolling-arc trajectories of the bimanual continuum robots A and B can be described as follows,

$$\begin{bmatrix} x_m \\ y_m \\ z_m \end{bmatrix}_{arc} = \begin{bmatrix} O_x \\ O_y - r(m) \times \cos \theta(m) \\ O_z - r(m) \times \sin \theta(m) \end{bmatrix} \quad (20)$$

where (20) can be used to compute the set of vector points $[x_m, y_m, z_m]^T_{arc}$ representing the robots’ tip coordinate positions along each of their rolling-arc trajectories. $[O_x, O_y, O_z]^T$ generally represents the center point coordinates of each arc trajectory. The angle θ ranges from 0 to π for each arc trajectory, whereas $m = 1, 2, 3, \dots, n$ is the dimensionless parameter that defines or parameterizes the arc trajectory points. $r(m)$ determines the radius at each point m of each arc trajectory.

Each of the rolling-arc trajectories is planned such that there is a continuous change (reduction) of radius along the arc trajectory points. That is, the initial radius $r(1)$ at the start-point of each arc trajectory continuously reduces to a smaller final radius $r(n)$ at the trajectory end-point. This is clearly illustrated in Fig. 5. For robot B’s arc trajectory I, the initial radius U at the start-point Be continuously reduces to a smaller final radius V at the trajectory end-point E1. V, which is now the initial radius at the start-point Ae of robot A’s arc trajectory II continuously reduces to a smaller final radius W at the trajectory end-point E2. W then becomes the initial radius at the start-point E1 of robot B’s arc trajectory III and continuously reduces to a smaller final radius X at the

trajectory end-point $E3$. Finally, X , which is now the initial radius at the start-point $E2$ of robot A 's arc trajectory IV , continuously reduces to a smaller final radius Y at the trajectory end-point $E4$. Effectively, there is a smooth and continuous change (reduction) of radius along the entire rolling-arc looping trajectories, i.e., the initial radius U continuously reduces to a final radius Y . Hence, the continuous or constant rate of change of the radius δr along the rolling-arc looping trajectories I , II , III , and IV can be stated as follows,

$$\delta r = \frac{U - V}{n} = \frac{V - W}{n} = \frac{W - X}{n} = \frac{X - Y}{n} = \frac{U - Y}{n \times R} \quad (21)$$

where n is the number of vector points along each arc trajectory and R is the total number of rolling-arc trajectories executed.

It is worth noting that the initial rolling-arc looping radius U indicates the length of the suture "leading" section initially held in tension by robot B that will be used or manipulated by both robots A and B during the rolling-arc looping process. Also, The final radius Y indicates the remaining length of the suture "leading" section kept in tension between robot B 's tip gripper at position $E3$ and the looping point C of robot arm A (with robot A 's tip gripper at position $E4$) at the end of the rolling-arc looping process (see Fig. 4 and Fig. 5). Therefore, the continuous or constant rate of change (reduction) δr of the looping radius from U to Y equals the rate of change (reduction) of the length of the suture "leading" section being looped around robot arm A . This allows the appropriate suture tension to be kept constant throughout the entire rolling-arc looping process to prevent the over-tensioning of the suture to avoid any breakage and the under-tensioning of the suture to avoid any sudden slippages and tangling.

The final radius Y is a critical parameter that is appropriately defined (selected) during the initial trajectory planning because it serves as a clearance to ensure collision-free between the bimanual continuum robots A and B at the end of the rolling-arc looping process. Therefore, with Y appropriately defined (selected), the initial looping radius U can be determined to ensure a collision-free suture looping process as follows,

$$U = Y + (\pi \times d_A \times R) \quad (22)$$

where d_A represents the miniature diameter of robot arm A around which the suture loops are formed. The final radius Y (selected) and the computed initial radius U can be substituted into (21) to determine the continuous or constant rate of change of radius δr along the rolling-arc looping trajectory. With δr determined, the radius $r(m)$ at each point m of each arc trajectory defined in (20) can be computed as follows,

$$r(m) = r(m - 1) - \delta r \quad (23)$$

2) Suture Tail Grasping and Unlooping for Knot Forming:

At the end of the rolling-arc looping process, the bimanual continuum robots A and B are at tip positions $E4$ and $E3$, respectively. What follows this process is the simultaneous movement by both robots A and B from tip positions $E4$ and $E3$ along the sequence of trajectories $E4-G$, $G-a$, $a-b$, $b-d$ and $E3-F$, $F-1$, $1-2$, $2-3$, $3-4$, respectively, as illustrated in Fig. 4 for the suture "tail" point grasping and lifting and the unlooping for knot forming and tightening processes. This sequence of linear trajectory planning follows a similar pattern to the one described in the spiral looping-based knot-tying trajectory planning approach in Sections III-A2 and III-A3. Compare the sequence of linear trajectories following the suture looping processes illustrated in Fig. 4 and Fig. 2 to see the similarity. Hence, (19) can be used to describe robot A 's linear trajectories $E4-G$, $G-a$, $a-b$, $b-d$ and robot B 's linear trajectories $E3-F$, $F-1$, $1-2$, $2-3$, $3-4$ following the rolling-arc looping process for the suture "tail" point grasping and lifting and the unlooping for knot forming and tightening processes.

IV. COOPERATIVE CONTROL SCHEME IMPLEMENTATION FOR AUTOMATED KNOT-TYING

Our cooperative control scheme focuses on ensuring seamless collaboration and synchronous operation of the bimanual continuum robots A and B in precisely tracking the pre-planned (reference) knot-tying trajectories. First, we implement in MATLAB the two scenarios of the automated knot-tying trajectory planning for the bimanual continuum robots described in Sections III-A and III-B. These pre-planned knot-tying trajectories are then translated into a set of vector points, which serve as the reference trajectory inputs for the control system. Based on the Jacobian transpose kinematic algorithms formulated in Section II-D, we have developed our cooperative control scheme as shown in Fig. 6. This cooperative control scheme, implemented using MATLAB/Simulink, allows the bimanual continuum robots A and B to track the reference (pre-planned) knot-tying trajectories collaboratively and precisely in environments and conditions typical in surgical settings.

As explained earlier in Section II-D, this Jacobian-based control scheme in Fig. 6 solves the kinematic control problem of the bimanual continuum robots A and B by incrementally finding the configuration velocities $\dot{\mathbf{q}}_A$ and $\dot{\mathbf{q}}_B$, which are integrated over time to compute the suitable set of configurations \mathbf{q}_A and \mathbf{q}_B in which the robots move to ensure smooth and precise tracking of the reference (pre-planned) knot-tying trajectories. $\mathbf{J}_{\mathbf{q}_A}^T$ and $\mathbf{J}_{\mathbf{q}_B}^T$ are the transpose of the robots' analytical Jacobians. $(\mathbf{K}_A \times \mathbf{e}_A)$ and $(\mathbf{K}_B \times \mathbf{e}_B)$ are called the feedback correction terms, which essentially eliminate any numerical drift that may occur in the solution. \mathbf{e}_A and \mathbf{e}_B are the tracking errors between the set of reference knot-tying trajectories $\mathbf{X}_{A(r)}$ and $\mathbf{X}_{B(r)}$ and the set of actual knot-tying trajectories $\mathbf{X}_{A(a)}$ and $\mathbf{X}_{B(a)}$ of robots A and B , respectively.

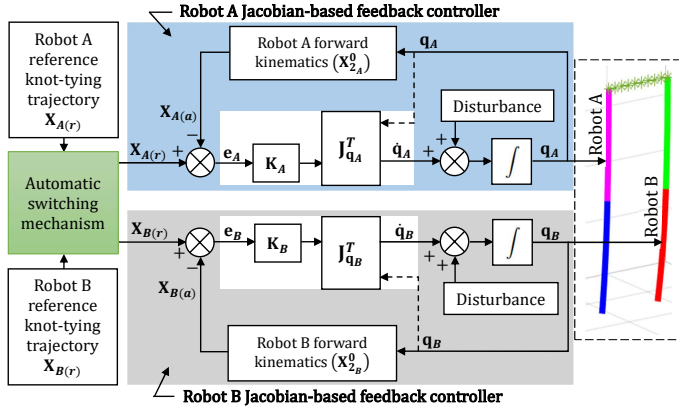


Fig. 6. The block diagram of the cooperative control scheme implemented for bimanual continuum robots for automated knot-tying tasks. $\mathbf{X}_{A(r)}$ and $\mathbf{X}_{B(r)}$ are the set of reference knot-tying trajectory points to be tracked by the bimanual continuum robots A and B , respectively. $\mathbf{X}_{A(a)}$ and $\mathbf{X}_{B(a)}$ are the set of actual knot-tying trajectory points generated by robots A and B , respectively. \mathbf{e}_A and \mathbf{e}_B are the set of trajectory tracking errors, whereas \mathbf{K}_A and \mathbf{K}_B are the controller gains for robots A and B , respectively. $\mathbf{J}_{q_A}^T$ and $\mathbf{J}_{q_B}^T$ are the transpose of the analytical Jacobian matrices for robots A and B , respectively. $\dot{\mathbf{q}}_A$ and $\dot{\mathbf{q}}_B$ are the configuration velocities generated by robots A and B , which are integrated over time to compute the suitable set of configurations \mathbf{q}_A and \mathbf{q}_B in which robots A and B move to ensure smooth and accurate knot-tying trajectory tracking. The automatic switching mechanism ensures the collaborative and synchronous movements of the bimanual continuum robots A and B during the knot-tying trajectory tracking process.

\mathbf{K}_A and \mathbf{K}_B are the suitably selected positive definite controller gains for proper tuning to ensure a stable control system with faster convergence rates and errors approaching zero.

In this research, we have implemented the pattern search optimization algorithm (`patternsearch(.)`) using MATLAB to simultaneously compute the optimized, positive definite, and diagonal gain matrices \mathbf{K}_A and \mathbf{K}_B during the simulation with the objective function of minimizing the trajectory tracking errors \mathbf{e}_A and \mathbf{e}_B . Pattern search, being a non-gradient (derivative-free) vector optimization algorithm, is effective in handling multiple and nonlinear objective functions [80].

The functionality of the automatic switching mechanism implemented in our cooperative control scheme ensures seamless collaboration and synchronous operation of the bimanual continuum robots by activating and deactivating their motions at specific time intervals and tip positions during the knot-tying trajectory tracking process. This delicate interplay between the bimanual continuum robots A and B is demonstrated through flow charts in Fig. 7 and Fig. 8 for the spiral looping-based knot-tying process (described in Section III-A) and the rolling-arc looping-based knot-tying process (described in Section III-B), respectively.

V. SIMULATION RESULTS AND DISCUSSION

In what follows, we have illustrated the effectiveness of our cooperative control scheme through simulation studies using MATLAB/Simulink. In the simulation analysis, we select the fixed arc length parameter (already assumed in the kinematics

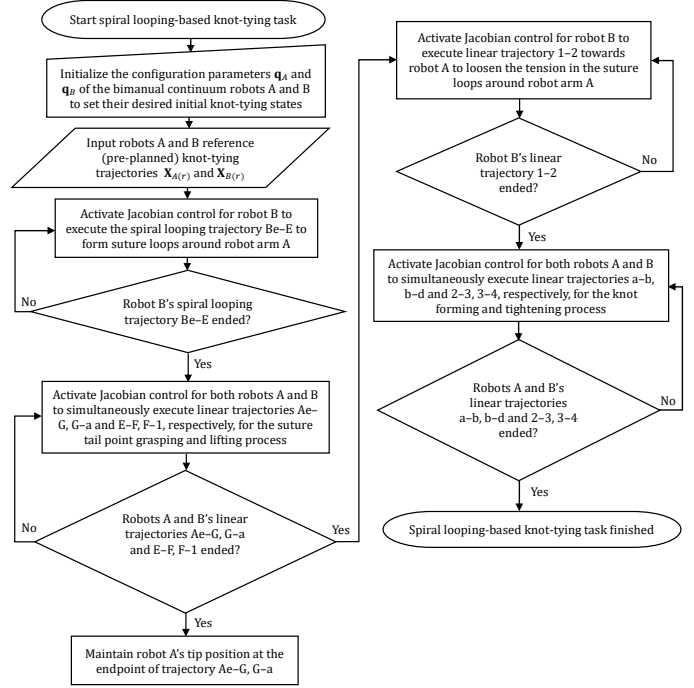


Fig. 7. Flow chart of the bimanual robots A and B 's collaborative control for the spiral looping-based automated knot-tying procedure.

modeling) for each section of the bimanual continuum robot arms A and B to be 0.2 m. Fig. 9 shows a MATLAB plot of the proposed two-section bimanual continuum robot arms A and B for visualization purposes.

A. Individual Continuum Robot Trajectory Tracking Test

Before evaluating our proposed cooperative control for the automated knot-tying, first, we implement the individual Jacobian-based controllers for each of the two-section bimanual continuum robots A and B to follow the typical sine wave reference trajectory in task space. This preliminary trajectory tracking test validates the effectiveness of the individual Jacobian transpose kinematic control algorithms in solving the kinematic control problem of each continuum robot. The initial values of continuum robots A 's configuration parameters \mathbf{q}_{0A} and continuum robots B 's configuration parameters \mathbf{q}_{0B} are arbitrarily selected as $\mathbf{q}_{0A} = (0.01, 0.02, 0.1, 0.05)$ and $\mathbf{q}_{0B} = (0.3, 0, 0.5, 0)$. The optimized controller gains for continuum robot A and continuum robot B are computed as $\mathbf{K}_A = \text{diag}[999800, 999944, 999998]$ and $\mathbf{K}_B = \text{diag}[999938, 999936, 999998]$, respectively, using the pattern search optimization algorithm mentioned earlier.

Fig. 10 and Fig. 11 show the trajectory tracking performance of continuum robot A and continuum robot B , respectively. As seen from Fig. 10 and Fig. 11, the actual tip trajectories of continuum robot A and continuum robot B follow the

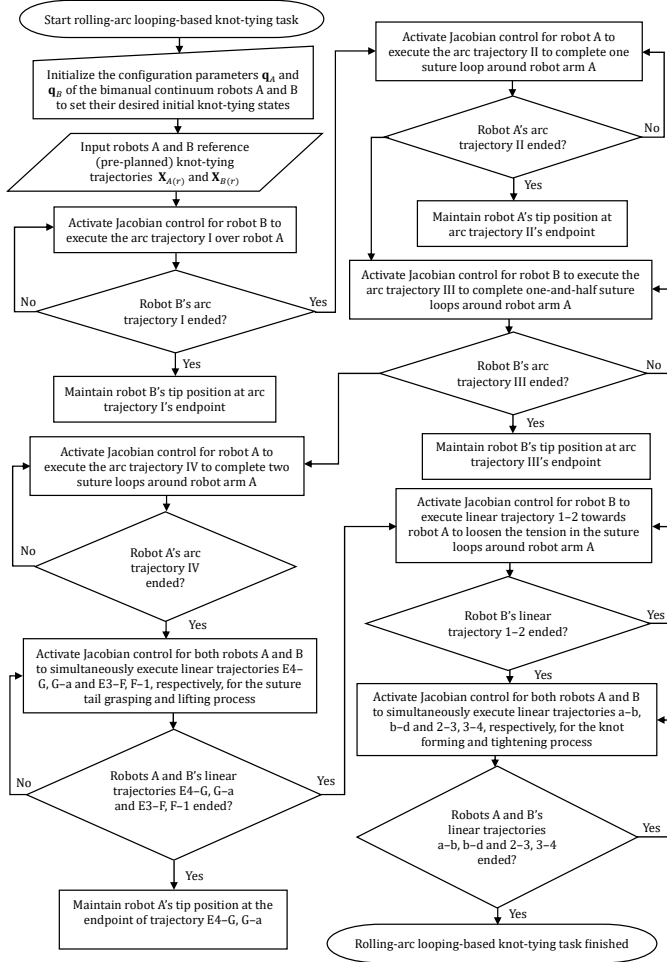


Fig. 8. Flow chart of the bimanual robots *A* and *B*'s collaborative control for the rolling-arc looping-based automated knot-tying procedure.

reference trajectories precisely, indicating that our proposed Jacobian-based control scheme is stable and guarantees faster convergence of the tracking errors. The root-mean-square errors (RMSE) are computed as 0.0021 m and 0.0020 m for continuum robot *A* and continuum robot *B*, respectively, indicating better tracking accuracy.

However, as seen from Fig. 10 and Fig. 11, significant errors occur at the beginning of the trajectory tracking process. This is due to the desired initial tip positions of the continuum robots that are unknown to the control system. In other words, the initial values of the configuration parameters $\mathbf{q}_{0_A} = (0.01, 0.02, 0.1, 0.05)$ and $\mathbf{q}_{0_B} = (0.3, 0, 0.5, 0)$ arbitrarily selected to initialize continuum robot *A* and continuum robot *B*'s trajectory tracking process do not correspond to the desired initial tip positions of the robots. This can be easily mitigated by initializing the simulation process using the configuration parameters that correspond to the desired initial tip positions of the robots. On the other hand, this demonstrates our control

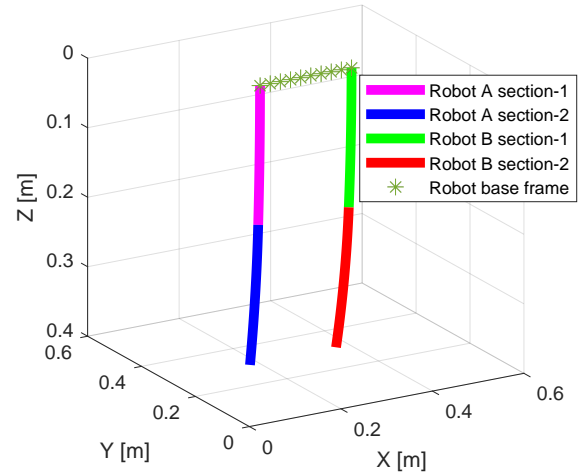


Fig. 9. The proposed two-section bimanual continuum robot arms *A* and *B* plotted in MATLAB by implementing the robots' forward kinematics. The configuration parameters for arm *A* and arm *B* are assumed as $\mathbf{q}_A = (0.01, 0.02, 0.1, 0.05)$ and $\mathbf{q}_B = (0.3, 0, 0.5, 0)$, respectively, for visualization purposes. The fixed arc length for each section is selected to be 0.2 m.

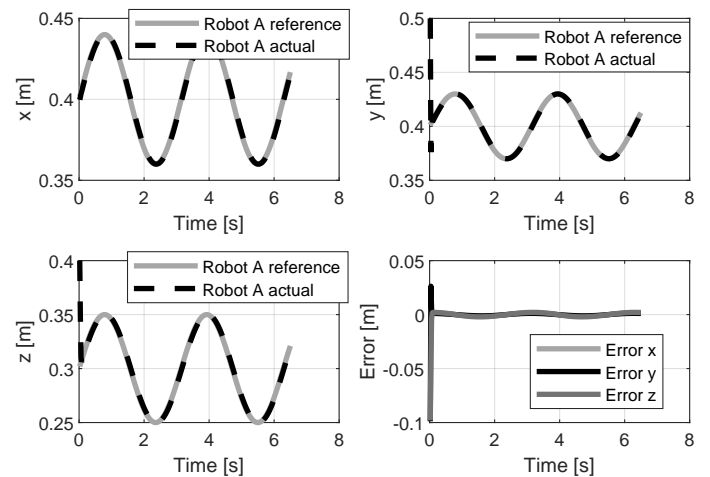


Fig. 10. Continuum robot *A*'s trajectory tracking performance. The optimized controller gain, $\mathbf{K}_A = \text{diag}[999800, 999944, 999998]$. The root-mean-square error (RMSE) computed is 0.0021 m.

system's ability to track complex trajectories by initializing the robot from any arbitrary initial tip position despite the mismatch that may occur between the desired and the actual initial tip positions of the robot. These results guarantee that the developed kinematics of the two-section bimanual continuum robots align with the Jacobian transpose kinematic algorithm.

B. Collaborative Knot-tying Trajectory Tracking Performance of Bimanual Continuum Robots

1) Spiral Looping-based Knot-tying Trajectory Tracking:

In this case, the initial values of the two-section bimanual continuum robots *A* and *B*'s configuration parameters \mathbf{q}_{0_A} and \mathbf{q}_{0_B} are arbitrarily selected as $\mathbf{q}_{0_A} = (0.1, 0, 0.15, 0.25)$

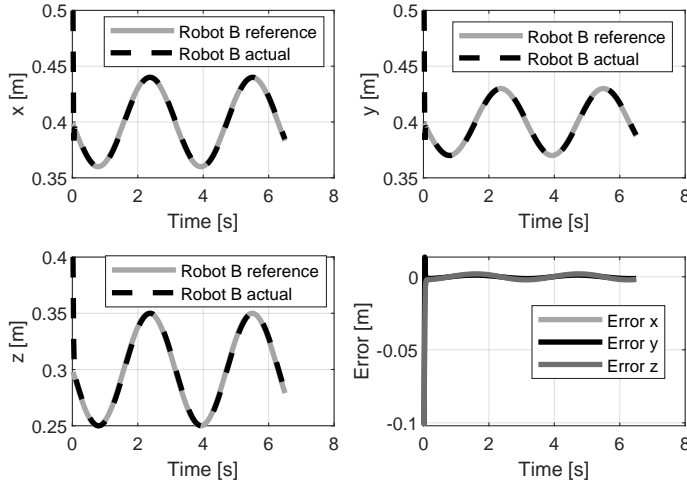


Fig. 11. Continuum robot B's trajectory tracking performance. The optimized controller gain, $\mathbf{K}_B = \text{diag}[999938, 999936, 999998]$. The root-mean-square error (RMSE) computed is 0.0020 m.

and $\mathbf{q}_{0B} = (0.25, 0.3, 0.35, 0.5)$. The optimized controller gains for continuum robot A and continuum robot B are computed as $\mathbf{K}_A = \text{diag}[1000000, 994518, 1000000]$ and $\mathbf{K}_B = \text{diag}[664576, 996242, 999968]$, respectively, using the pattern search optimization algorithm mentioned earlier. Results of the collaborative spiral looping-based knot-tying trajectory tracking performance of the bimanual continuum robots A and B without any perturbation are shown in Fig. 12 and Fig. 13. We have also evaluated the collaborative trajectory tracking performance of bimanual continuum robots A and B against a pulse disturbance of magnitude $[70, 68, 90, 80]^T$ added to robot B's the control signal $\dot{\mathbf{q}}_B$; and the results obtained are as shown in Fig. 14 and Fig. 15.

The results in Fig. 12, Fig. 13, Fig. 14, and Fig. 15 not only demonstrate the seamless interplay (collaboration) and synchronous operation of the bimanual continuum robots A and B in precisely tracking the reference (pre-planned) spiral looping-based knot-tying trajectories but also highlight the stability and robustness of our cooperative control system against perturbation, particularly pulse disturbances (see Fig. 14 and Fig. 15), which may occur in surgical settings. These results reinforce the reliability of our proposed cooperative control scheme, which guarantees faster convergence of the tracking errors. The root-mean-square errors (RMSE) of the bimanual continuum robots A and B are computed as 0.0004 m and 0.0016 m, respectively, indicating better tracking accuracy.

2) *Rolling-arc Looping-based Knot-tying Trajectory Tracking*: In the case of rolling-arc looping-based knot-tying, the initial values of the two-section bimanual continuum robots A and B's configuration parameters \mathbf{q}_{0A} and \mathbf{q}_{0B} are arbitrarily selected as $\mathbf{q}_{0A} = (0.13, 0.9, 0.4, 0.1)$ and $\mathbf{q}_{0B} = (0.3, 0.14, 0.8, 0.65)$. The optimized controller gains for continuum robot A and continuum robot B are com-

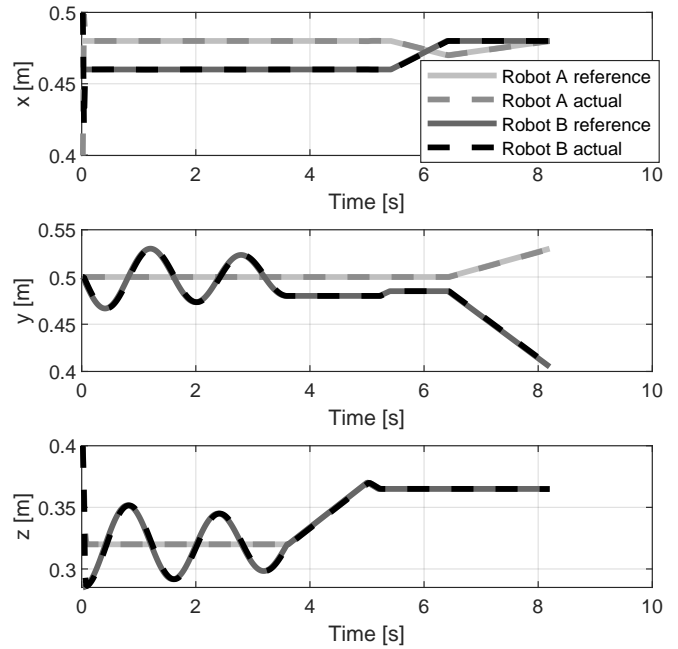


Fig. 12. Results of the collaborative spiral looping-based knot-tying trajectory tracking performance of bimanual continuum robots A and B without perturbation.

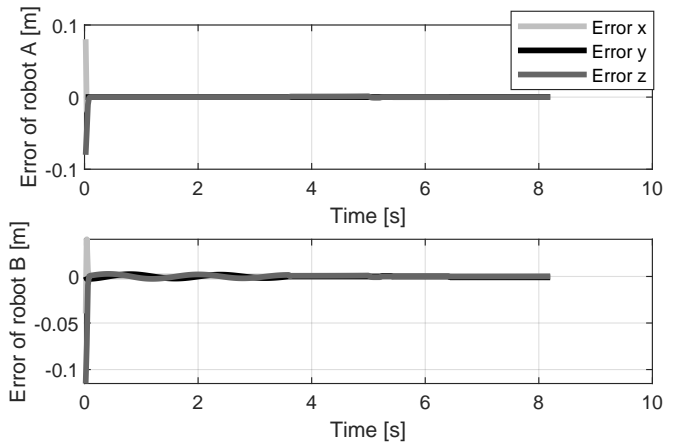


Fig. 13. Tracking errors between the reference and the actual spiral looping-based knot-tying trajectories without perturbation.

puted as $\mathbf{K}_A = \text{diag}[998396, 995840, 1000000]$ and $\mathbf{K}_B = \text{diag}[999982, 999424, 999998]$, respectively, using the pattern search optimization algorithm mentioned earlier. Results of the collaborative rolling-arc looping-based knot-tying trajectory tracking performance of the bimanual continuum robots A and B with no perturbation are shown in Fig. 16 and Fig. 17. Furthermore, we have evaluated the collaborative trajectory tracking performance of bimanual continuum robots A and B against pulse disturbances of magnitudes $[40, 35, 75, 60]^T$

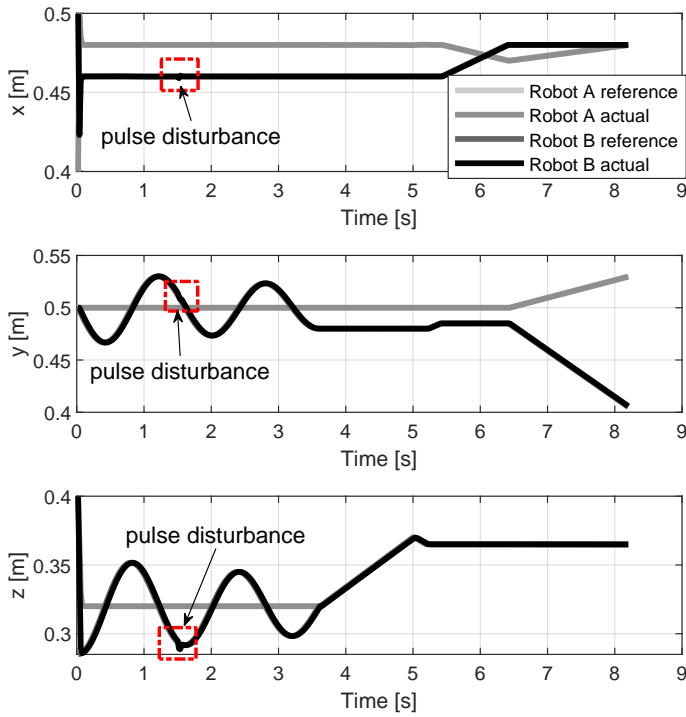


Fig. 14. Results of the collaborative spiral looping-based knot-tying trajectory tracking performance of bimanual continuum robots *A* and *B* with perturbation. The magnitude of pulse disturbance added to the system's control signal $\dot{\mathbf{q}}_B$ is $[70, 68, 90, 80]^T$.

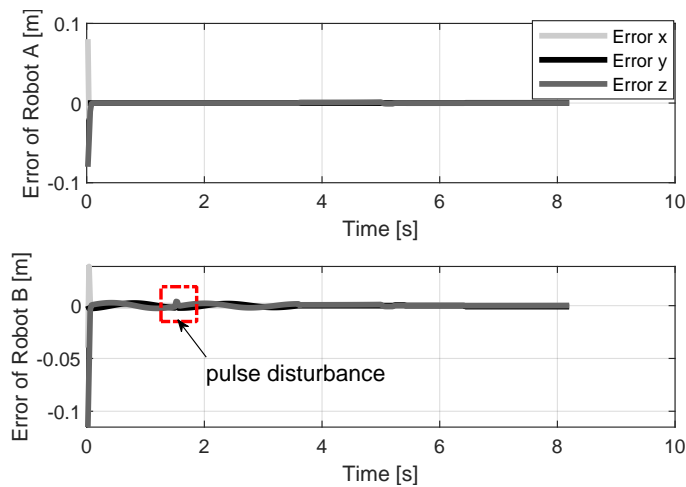


Fig. 15. Tracking errors between the reference and the actual spiral looping-based knot-tying trajectories with perturbation. The magnitude of pulse disturbance added to the system's control signal $\dot{\mathbf{q}}_B$ is $[70, 68, 90, 80]^T$.

and $[70, 68, 90, 80]^T$ added to both robot *A* robot *B*'s control signals $\dot{\mathbf{q}}_A$ and $\dot{\mathbf{q}}_B$, respectively. The corresponding results obtained are as shown in Fig. 18 and Fig. 19.

The results in Fig. 16 and Fig. 17 demonstrate seamless interplay (collaboration) between the bimanual continuum robots *A* and *B* as well as their synchronous operation in precisely tracking the reference (pre-planned) rolling-arc looping-based

knot-tying trajectories. Furthermore, the results in Fig. 18 and Fig. 19 showcase the cooperative control system's stability and superior robustness against perturbations, particularly pulse disturbances of increased magnitudes. These results reinforce the reliability of our proposed cooperative control scheme, which guarantees faster convergence of the tracking errors. The root-mean-square errors (RMSE) of the bimanual continuum robots *A* and *B* are computed as 0.0010 m and 0.0012 m, respectively, indicating better tracking accuracy.

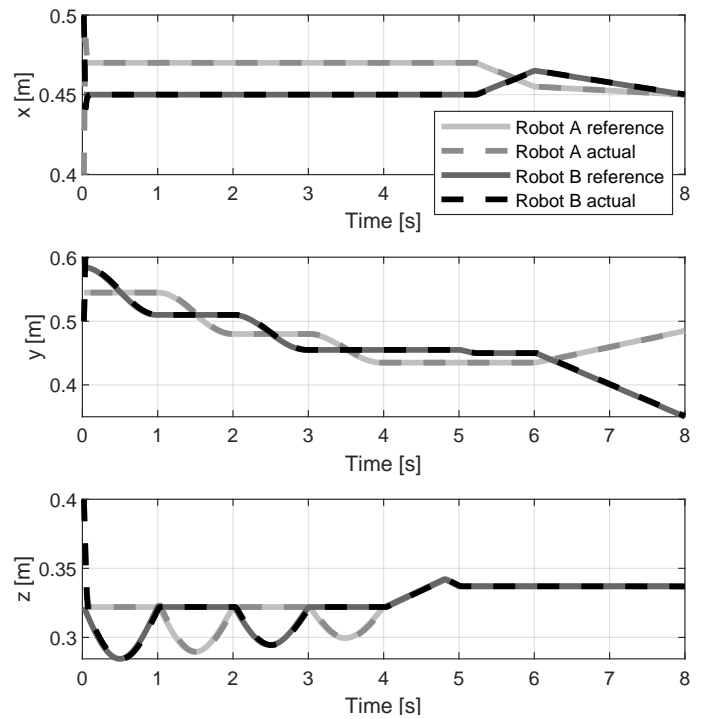


Fig. 16. Results of the collaborative rolling-arc looping-based knot-tying trajectory tracking performance of bimanual continuum robots *A* and *B* without perturbation.

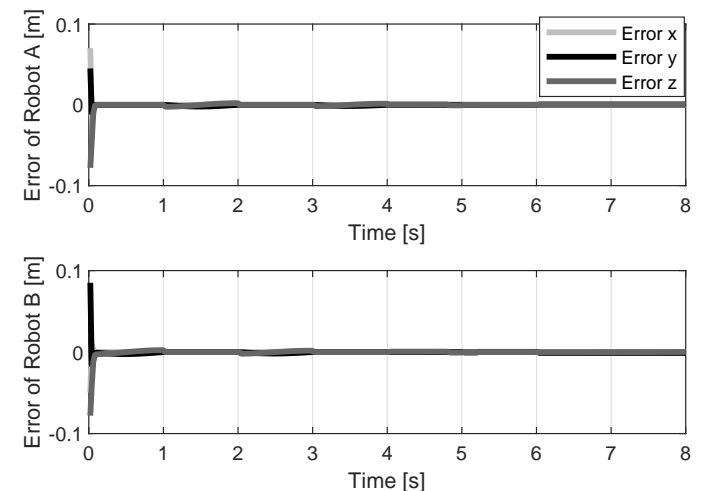


Fig. 17. Tracking errors between the reference and the actual rolling-arc looping-based knot-tying trajectories without perturbation.

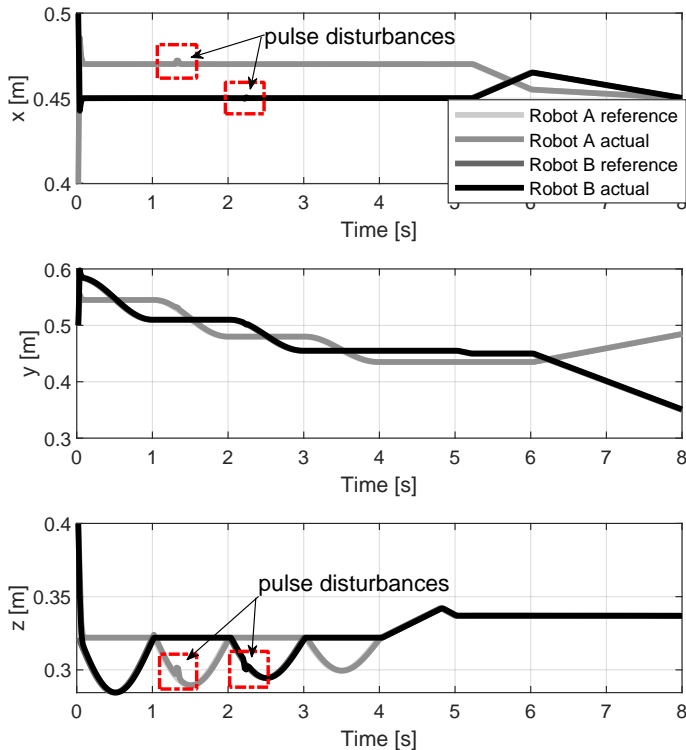


Fig. 18. Results of the collaborative spiral looping-based knot-tying trajectory tracking performance of bimanual continuum robots *A* and *B* with perturbation. The magnitude of pulse disturbance added to the control signals $\dot{\mathbf{q}}_A$ and $\dot{\mathbf{q}}_B$ are $[40, 35, 75, 60]^T$ and $[70, 68, 90, 80]^T$, respectively.

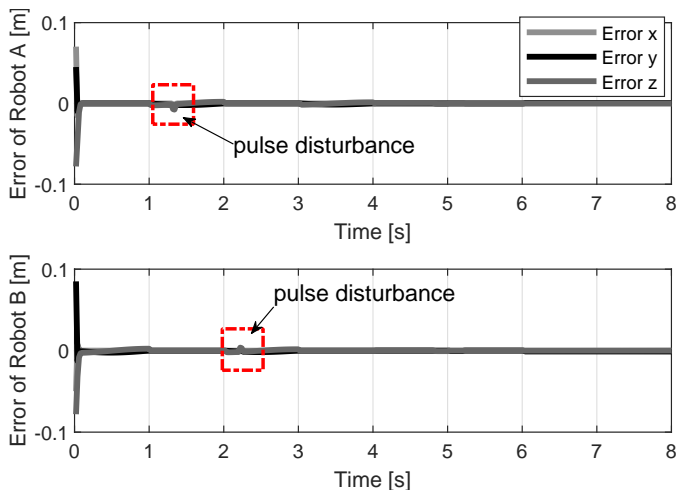


Fig. 19. Tracking errors between the reference and the actual rolling-arc looping-based knot-tying trajectories with perturbation. The magnitude of pulse disturbance added to the control signals $\dot{\mathbf{q}}_A$ and $\dot{\mathbf{q}}_B$ are $[40, 35, 75, 60]^T$ and $[70, 68, 90, 80]^T$, respectively.

C. Monte Carlo Robustness Analysis

The robustness of the cooperative control approach is a key evaluation element in automated RAMIS procedures. Based on both knot-tying cases, we have performed Monte Carlo simu-

lations to analyze the robustness of the proposed cooperative control approach against varying levels of pulse disturbances that could occur in surgical settings. In the analysis, ten different scenarios of simulation experiments are performed, and in each experimental scenario, varying levels of pulse disturbances are added to both control signals $\dot{\mathbf{q}}_A$ and $\dot{\mathbf{q}}_B$ (see Table I, where $\hat{\kappa}$ and $\hat{\phi}$ parameters are measured in $m^{-1}s^{-1}$ and $rads^{-1}$ respectively). Subsequently, for each experimental scenario, we have computed the Sum of the Root Mean Square Error (SRMSE) of the bimanual continuum robots in both the spiral looping-based knot-tying and the rolling-arc looping-based knot-tying trajectory tracking cases, as illustrated in Fig. 20. The results, as seen from Fig. 20, indicate that in all the ten different scenarios of the Monte Carlo simulations conducted for each knot-tying case, the computed SRMSE values remained approximately the same or unchanged despite the varying and increasing levels of disturbances introduced into the system. This demonstrates the developed cooperative control system’s superior robustness against varying or rising levels of pulse disturbances that could exist.

TABLE I. TEN SCENARIOS OF VARYING DISTURBANCE LEVELS INTRODUCED INTO THE CONTROL SYSTEM FOR THE MONTE CARLO SIMULATIONS

Scenario	$\dot{\mathbf{q}}_A$				$\dot{\mathbf{q}}_B$			
	$\hat{\kappa}_1$	$\hat{\phi}_1$	$\hat{\kappa}_2$	$\hat{\phi}_2$	$\hat{\kappa}_1$	$\hat{\phi}_1$	$\hat{\kappa}_2$	$\hat{\phi}_2$
1	3	2	5	4	7	6	9	8
2	6	4	10	8	14	12	18	16
3	9	6	15	12	21	18	27	24
4	12	8	20	16	28	24	36	32
5	15	10	25	20	35	30	45	40
6	20	15	35	28	42	38	54	48
7	25	20	45	36	49	46	63	56
8	30	25	55	44	56	54	72	64
9	35	30	65	52	63	60	81	72
10	40	35	75	60	70	68	90	80

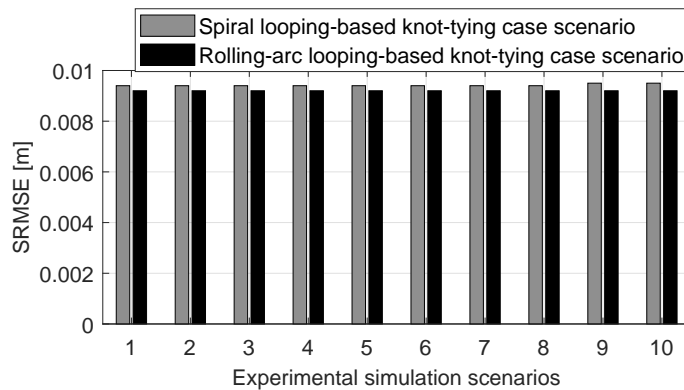


Fig. 20. Monte Carlo robustness performance of the proposed cooperative control system.

VI. CONCLUSION AND FUTURE WORKS

Through meticulous trajectory planning and the cooperative control scheme developed based on the Jacobian transpose

kinematic algorithms, we have successfully simulated two-section bimanual continuum robots' seamless collaboration and synchronous operation for automated knot-tying tasks in environments and conditions typical in surgical settings, ensuring their precise knot-tying trajectory tracking performance. The effectiveness of our cooperative control scheme has been illustrated through simulation studies using MATLAB/Simulink in terms of trajectory tracking performance. Meanwhile, ten Monte Carlo simulations have been conducted to analyze the system's robustness against pulse disturbances that could occur in surgical settings. All ten simulations returned approximately the same error values despite the increasing disturbance levels applied. The results have not only demonstrated the seamless collaboration and synchronous operation of the bimanual continuum robots in precisely tracking the pre-planned knot-tying trajectories with errors less than 0.0017 m but also highlighted the stability, effective tuning (guaranteeing faster convergence of the tracking errors) and robustness of our cooperative control system against varying levels of pulse disturbances. This study demonstrates precision, robustness, and autonomy in bimanual continuum robotic knot-tying in RAMIS, promising safe robot-patient interaction and reduced surgeon workload and surgery time, thus highlighting the significant contributions of this research to the field.

In the future, our cooperative control strategy will incorporate Model Predictive Control (MPC) to integrate motion constraints on the bimanual continuum robots' tips and actuators. This will allow the robots to collaborate and coordinate their distal tip motions while avoiding collision or interference that could occur between the robot arms due to a disturbance causing a change in the robot configurations. With MPC, a collision-free workspace could be respected while achieving the automated knot-tying task. Furthermore, we will implement a prototype of the physical system to experimentally validate the MPC-based cooperative control strategy tailored for automated knot-tying.

DECLARATION

The authors declare that they do not have any conflict of interest in this research and that no financial support was received during the manuscript preparation.

REFERENCES

- [1] P. E. Dupont *et al.*, "A decade retrospective of medical robotics research from 2010 to 2020," *Science robotics*, vol. 6, no. 60, 2021, doi: 10.1126/scirobotics.abi8017.
- [2] K. Kawashima, T. Kanno, and K. Tadano, "Robots in laparoscopic surgery: current and future status," *BMC Biomedical Engineering*, vol. 1, no. 12, pp. 1–6, 2019, doi: 10.1186/s42490-019-0012-1.
- [3] K. R. Sheth and C. J. Koh, "The future of robotic surgery in pediatric urology: Upcoming technology and evolution within the field," *Frontiers in Pediatrics*, vol. 7, p. 259, 2019, doi: 10.3389/fped.2019.00259.
- [4] T. Haidegger and J. Sándor, "Robot-assisted minimally invasive surgery in the age of surgical data science," *Magyar Sebeszet*, vol. 74, no. 4, pp. 127–135, 2021, doi: 10.1556/1046.74.2021.4.5.
- [5] J. Klodmann *et al.*, "An introduction to robotically assisted surgical systems: Current developments and focus areas of research," *Current Robotics Reports*, vol. 2, no. 3, pp. 321–332, 2021, doi: 10.1007/s43154-021-00064-3.
- [6] G. Dagnino and D. Kundrat, "Robot-assistive minimally invasive surgery: trends and future directions," *International Journal of Intelligent Robotics and Applications*, pp. 1–15, 2024, doi: 10.1007/s41315-024-00341-2.
- [7] P. Probst, "A review of the role of robotics in surgery: To davinci and beyond!," *Missouri Medicine*, vol. 120, no. 5, pp. 389–396, 2023.
- [8] L. Cao *et al.*, "Sewing up the wounds: A robotic suturing system for flexible endoscopy," *IEEE Robotics & Automation Magazine*, vol. 27, no. 3, pp. 45–54, 2020, doi: 10.1109/MRA.2019.2963161.
- [9] A. Attanasio, B. Scaglioni, E. De Momi, P. Fiorini, and P. Valdastrì, "Autonomy in surgical robotics," *Annual Review of Control, Robotics, and Autonomous Systems*, vol. 4, pp. 651–679, 2021, doi: 10.1146/annurev-control-062420-090543.
- [10] M. M. Marinho, K. Harada, A. Morita, and M. Mitsuishi, "Smartarm: Integration and validation of a versatile surgical robotic system for constrained workspaces," *The International Journal of Medical Robotics and Computer Assisted Surgery*, vol. 16, no. 2, 2020, doi: 10.1002/rcs.2053.
- [11] M. M. Marinho, K. Harada, K. Deie, T. Ishimaru, and M. Mitsuishi, "Smartarm: Suturing feasibility of a surgical robotic system on a neonatal chest model," *IEEE Transactions on Medical Robotics and Bionics*, vol. 3, no. 1, pp. 253–256, 2021, doi: 10.1109/TMRB.2021.3049878.
- [12] Y. Hu, W. Li, L. Zhang, and G.-Z. Yang, "Designing, prototyping, and testing a flexible suturing robot for transanal endoscopic microsurgery," *IEEE Robotics and Automation Letters*, vol. 4, no. 2, pp. 1669–1675, 2019, doi: 10.1109/LRA.2019.2896883.
- [13] A. Ehrampoosh, B. Shirinzadeh, J. Pinskiel, J. Smith, R. Moshinsky, and Y. Zhong, "A force-feedback methodology for teleoperated suturing task in robotic-assisted minimally invasive surgery," *Sensors*, vol. 22, no. 20, p. 7829, 2022, doi: 10.3390/s22207829.
- [14] I. El Rassi and J.-M. El Rassi, "A review of haptic feedback in teleoperated robotic surgery," *Journal of medical engineering & technology*, vol. 44, no. 5, pp. 247–254, 2020, doi: 10.1080/03091902.2020.1772391.
- [15] R. V. Patel, S. F. Atashzar, and M. Tavakoli, "Haptic feedback and force-based teleoperation in surgical robotics," *Proceedings of the IEEE*, vol. 110, no. 7, pp. 1012–1027, 2022, doi: 10.1109/JPROC.2022.3180052.
- [16] E. Abdi, D. Kulić, and E. Croft, "Haptics in teleoperated medical interventions: Force measurement, haptic interfaces and their influence on user's performance," *IEEE Transactions on Biomedical Engineering*, vol. 67, no. 12, pp. 3438–3451, 2020, doi: 10.1109/TBME.2020.2987603.
- [17] D. Zhang, W. Si, W. Fan, Y. Guan, and C. Yang, "From teleoperation to autonomous robot-assisted microsurgery: A survey," *Machine Intelligence Research*, vol. 19, no. 4, pp. 288–306, 2022, doi: 10.1007/s11633-022-1332-5.
- [18] T. Haidegger, "Autonomy for surgical robots: Concepts and paradigms," *IEEE Transactions on Medical Robotics and Bionics*, vol. 1, no. 2, pp. 65–76, 2019, doi: 10.1109/TMRB.2019.2913282.
- [19] A. A. Gumbs *et al.*, "Artificial intelligence surgery: How do we get to autonomous actions in surgery?" *Sensors*, vol. 21, no. 16, p. 5526, 2021, doi: 10.3390/s21165526.
- [20] F. Richter *et al.*, "Autonomous robotic suction to clear the surgical field for hemostasis using image-based blood flow detection," *IEEE Robotics and Automation Letters*, vol. 6, no. 2, pp. 1383–1390, 2021, doi: 10.1109/LRA.2021.3056057.
- [21] A. Attanasio *et al.*, "Autonomous tissue retraction in robotic assisted minimally invasive surgery—a feasibility study," *IEEE Robotics and Automation Letters*, vol. 5, no. 4, pp. 6528–6535, 2020, doi: 10.1109/LRA.2020.3013914.
- [22] G. Fagogenis *et al.*, "Autonomous robotic intracardiac catheter navigation using haptic vision," *Science robotics*, vol. 4, no. 29, 2019, doi: 10.1126/scirobotics.aaw1977.
- [23] H. Saeidi *et al.*, "Autonomous robotic laparoscopic surgery for intestinal anastomosis," *Science robotics*, vol. 7, no. 62, 2022, doi: 10.1126/scirobotics.abj2908.
- [24] S. A. Pedram *et al.*, "Autonomous suturing framework and quantification using a cable-driven surgical robot," *IEEE Transactions on Robotics*, vol. 37, no. 2, pp. 404–417, 2020, doi: 10.1109/TRO.2020.3031236.

- [25] T. D. Nagy and T. Haidegger, "A dvrk-based framework for surgical subtask automation," *Acta Polytechnica Hungarica*, vol. 16, no. 8, pp. 61–78, 2019, doi: 10.12700/aph.16.8.2019.8.5
- [26] H. Su, A. Mariani, S. E. Ovrur, A. Menciasci, G. Ferrigno, and E. De Momi, "Toward teaching by demonstration for robot-assisted minimally invasive surgery," *IEEE Transactions on Automation Science and Engineering*, vol. 18, no. 2, pp. 484–494, 2021, doi: 10.1109/TASE.2020.3045655.
- [27] M. Wagner *et al.*, "A learning robot for cognitive camera control in minimally invasive surgery," *Surgical Endoscopy*, vol. 35, no. 9, pp. 5365–5374, 2021, doi: 10.1007/s00464-021-08509-8.
- [28] B. Lu, X. Yu, J. Lai, K. Huang, K. C. Chan, and H. K. Chu, "A learning approach for suture thread detection with feature enhancement and segmentation for 3-d shape reconstruction," *IEEE Transactions on Automation Science and Engineering*, vol. 17, no. 2, pp. 858–870, 2019, doi: 10.1109/TASE.2019.2950005.
- [29] B. Lu, H. K. Chu, K. Huang, and J. Lai, "Surgical suture thread detection and 3-d reconstruction using a model-free approach in a calibrated stereo visual system," *IEEE/ASME Transactions on Mechatronics*, vol. 25, no. 2, pp. 792–803, 2019, doi: 10.1109/TMECH.2019.2942715.
- [30] B. Lu *et al.*, "Toward image-guided automated suture grasping under complex environments: A learning-enabled and optimization-based holistic framework," *IEEE Transactions on Automation Science and Engineering*, vol. 19, no. 4, pp. 3794–3808, 2021, doi: 10.1109/TASE.2021.3136185.
- [31] B. Lu, H. K. Chu, K. C. Huang, and L. Cheng, "Vision-based surgical suture looping through trajectory planning for wound suturing," *IEEE Transactions on Automation Science and Engineering*, vol. 16, no. 2, pp. 542–556, 2019, doi: 10.1109/TASE.2018.2840532.
- [32] J. R. U. Roldan and D. Milutinović, "Suture looping task pose planner in a constrained surgical environment," *Journal of Intelligent & Robotic Systems*, vol. 106, no. 78, 2022, doi: 10.1007/s10846-022-01772-4.
- [33] P. R. Koninckx, A. Ussia, A. Wattiez, W. Kondo, and A. Romeo, "Laparoscopic surgery: A systematic review of loop and knot security, varying with the suture and sequences, throws, rotation and destabilization of half-knots or half-hitches," *Journal of Clinical Medicine*, vol. 12, no. 19, p. 6166, 2023, doi: 10.3390/jcm12196166.
- [34] A. Romeo, L. F. Fernandes, G. V. Cervantes, R. Botchorishvili, C. Benedetto, L. Adamyan, A. Ussia, A. Wattiez, W. Kondo, and P. R. Koninckx, "Which knots are recommended in laparoscopic surgery and how to avoid insecure knots," *Journal of Minimally Invasive Gynecology*, vol. 27, no. 6, pp. 1395–1404, 2020, doi: 10.1016/j.jmig.2019.09.782.
- [35] X. Qin *et al.*, "Beyond the square knot: A validation study for a novel knot-tying method named "inverse 9"," *Heliyon*, vol. 9, no. 10, 2023, doi: 10.1016/j.heliyon.2023.e20673.
- [36] O. Yasa *et al.*, "An overview of soft robotics," *Annual Review of Control, Robotics, and Autonomous Systems*, vol. 6, pp. 1–29, 2023, doi: 10.1146/annurev-control-062322-100607.
- [37] M. Runciman, A. Darzi, and G. P. Mylonas, "Soft robotics in minimally invasive surgery," *Soft robotics*, vol. 6, no. 4, pp. 423–443, 2019, doi: 10.1089/soro.2018.0136.
- [38] O. M. Omisore, S. Han, J. Xiong, H. Li, Z. Li, and L. Wang, "A review on flexible robotic systems for minimally invasive surgery," *IEEE Transactions on Systems, Man, and Cybernetics: Systems*, vol. 52, no. 1, pp. 631–644, 2020, doi: 10.1109/TSMC.2020.3026174.
- [39] S. Kolachalama *et al.*, "Continuum robots for manipulation applications: A survey," *Journal of Robotics*, vol. 2020, no. 4187048, p. 19, 2020, doi: 10.1155/2020/4187048.
- [40] S. Aracri *et al.*, "Soft robots for ocean exploration and offshore operations: A perspective," *Soft Robotics*, vol. 8, no. 6, pp. 625–639, 2021, doi: 10.1089/soro.2020.0011.
- [41] G. Li *et al.*, "Bioinspired soft robots for deep-sea exploration," *Nature Communications*, vol. 14, no. 1, p. 7097, 2023, doi: 10.1038/s41467-023-42882-3.
- [42] G. Li *et al.*, "Self-powered soft robot in the mariana trench," *Nature*, vol. 591, no. 7848, pp. 66–71, 2021, doi: 10.1038/s41586-020-03153-z.
- [43] M. M. Coad *et al.*, "Vine robots," *IEEE Robotics & Automation Magazine*, vol. 27, no. 3, pp. 120–132, 2019, doi: 10.1109/MRA.2019.2947538.
- [44] Y. Zhang and M. Lu, "A review of recent advancements in soft and flexible robots for medical applications," *The International Journal of Medical Robotics and Computer Assisted Surgery*, vol. 16, no. 3, 2020, doi: 10.1002/ics.2096.
- [45] H. Alfalahi, F. Renda, and C. Stefanini, "Concentric tube robots for minimally invasive surgery: Current applications and future opportunities," *IEEE Transactions on Medical Robotics and Bionics*, vol. 2, no. 3, pp. 410–424, 2020, doi: 10.1109/TMRB.2020.3000899.
- [46] W. Shen, G. Yang, T. Zheng, Y. Wang, K. Yang, and Z. Fang, "An accuracy enhancement method for a cable-driven continuum robot with a flexible backbone," *IEEE Access*, vol. 8, pp. 37474–37481, 2020, doi: 10.1109/ACCESS.2020.2975087.
- [47] E. Amanov, T.-D. Nguyen, and J. Burgner-Kahrs, "Tendon-driven continuum robots with extensible sections—a model-based evaluation of path-following motions," *The International Journal of Robotics Research*, vol. 40, no. 1, pp. 7–23, 2021, doi: 10.1177/0278364919886047.
- [48] M. T. Chikhaoui, S. Lilje, S. Kleinschmidt, and J. Burgner-Kahrs, "Comparison of modeling approaches for a tendon actuated continuum robot with three extensible segments," *IEEE Robotics and Automation Letters*, vol. 4, no. 2, pp. 989–996, 2019, doi: 10.1109/LRA.2019.2893610.
- [49] S. Grazioso, G. Di Gironimo, and B. Siciliano, "A geometrically exact model for soft continuum robots: The finite element deformation space formulation," *Soft robotics*, vol. 6, no. 6, pp. 790–811, 2019, doi: 10.1089/soro.2018.0047.
- [50] F. Janabi-Sharifi, A. Jalali, and I. D. Walker, "Cosserat rod-based dynamic modeling of tendon-driven continuum robots: A tutorial," *IEEE Access*, vol. 9, pp. 68 703–68 719, 2021, doi: 10.1109/ACCESS.2021.3077186.
- [51] C. Della Santina and D. Rus, "Control oriented modeling of soft robots: the polynomial curvature case," *IEEE Robotics and Automation Letters*, vol. 5, no. 2, pp. 290–298, 2019, doi: 10.1109/LRA.2019.2955936.
- [52] J. Lai, B. Lu, Q. Zhao, and H. K. Chu, "Constrained motion planning of a cable-driven soft robot with compressible curvature modeling," *IEEE Robotics and Automation Letters*, vol. 7, no. 2, pp. 4813–4820, 2022, doi: 10.1109/LRA.2022.3152318.
- [53] H. El-Hussieny, I. A. Hameed, and A. A. Nada, "Deep cnn-based static modeling of soft robots utilizing absolute nodal coordinate formulation," *Biomimetics*, vol. 8, no. 8, p. 611, 2023, doi: 10.3390/biomimetics8080611.
- [54] A. Nada and H. El-Hussieny, "Development of inverse static model of continuum robots based on absolute nodal coordinates formulation for large deformation applications," *Acta Mechanica*, pp. 1–23, 2023, doi: 10.1007/s00707-023-03814-w.
- [55] A. Amouri, "Investigation of the constant curvature kinematic assumption of a 2-dofs cable-driven continuum robot," *UPB Scientific Bulletin, Series D: Mechanical Engineering*, no. 3, pp. 27–38, 2019.
- [56] T. Xu, J. Zhang, M. Salehizadeh, O. Onaizah, and E. Diller, "Millimeter-scale flexible robots with programmable three-dimensional magnetization and motions," *Science Robotics*, vol. 4, no. 29, 2019, doi: 10.1126/scirobotics.aav4494.
- [57] I. A. Seleem, H. El-Hussieny, and H. Ishii, "Recent developments of actuation mechanisms for continuum robots: A review," *International Journal of Control, Automation and Systems*, vol. 21, pp. 1592–1609, 2023, doi: 10.1007/s12555-022-0159-8.
- [58] U. Gupta, L. Qin, Y. Wang, H. Godaba, and J. Zhu, "Soft robots based on dielectric elastomer actuators: A review," *Smart Materials and Structures*, vol. 28, no. 10, p. 103002, 2019, doi: 10.1088/1361-665X/ab3a77.
- [59] J.-H. Youn *et al.*, "Dielectric elastomer actuator for soft robotics applications and challenges," *Applied Sciences*, vol. 10, no. 2, p. 640, 2020, doi: 10.3390/app10020640.
- [60] Y. Kim, G. A. Parada, S. Liu, and X. Zhao, "Ferromagnetic soft continuum robots," *Science Robotics*, vol. 4, no. 33, 2019, doi: 10.1126/scirobotics.aax7329.
- [61] C. Della Santina, R. K. Katzschmann, A. Bicchi, and D. Rus, "Model-based dynamic feedback control of a planar soft robot: trajectory tracking and interaction with the environment," *The International Journal of Robotics Research*, vol. 39, no. 4, pp. 490–513, 2020, doi: 10.1177/0278364919897292.
- [62] X. Wang, Y. Li, and K.-W. Kwok, "A survey for machine learning-based control of continuum robots," *Frontiers in Robotics and AI*, vol. 8, p. 730330, 2021, doi: 10.3389/frobt.2021.730330.
- [63] I. A. Seleem, H. El-Hussieny, S. F. Assal, and H. Ishii, "Development and stability analysis of an imitation learning-based pose planning approach

- for multi-section continuum robot,” *IEEE Access*, vol. 8, pp. 99366–99379, 2020, doi: 10.1109/ACCESS.2020.2997636.
- [64] C. Della Santina, C. Duriez, and D. Rus, “Model-based control of soft robots: A survey of the state of the art and open challenges,” *IEEE Control Systems Magazine*, vol. 43, no. 3, pp. 30–65, 2023, doi: 10.1109/MCS.2023.3253419.
- [65] H. El-Hussieny, I. A. Hameed, and J.-H. Ryu, “Nonlinear model predictive growth control of a class of plant-inspired soft growing robots,” *IEEE Access*, vol. 8, pp. 214495–214503, 2020, doi: 10.1109/ACCESS.2020.3041616.
- [66] H. El-Hussieny, I. A. Hameed, and A. B. Zaky, “Plant-inspired soft growing robots: A control approach using nonlinear model predictive techniques,” *Applied Sciences*, vol. 13, no. 4, p. 2601, 2023, doi: 10.3390/app13042601.
- [67] I. A. Seleem, H. El-Hussieny, and H. Ishii, “Imitation-based path planning and nonlinear model predictive control of a multi-section continuum robots,” *Journal of Intelligent & Robotic Systems*, vol. 108, no. 9, pp. 1–13, 2023, doi: 10.1007/s10846-023-01811-8.
- [68] I. A. Seleem, S. F. Assal, H. Ishii, and H. El-Hussieny, “Guided pose planning and tracking for multi-section continuum robots considering robot dynamics,” *IEEE Access*, vol. 7, pp. 166690–166703, 2019, doi: 10.1109/ACCESS.2019.2953122.
- [69] I. A. Seleem, H. El-Hussieny, and H. Ishii, “Imitation-based motion planning and control of a multi-section continuum robot interacting with the environment,” *IEEE Robotics and Automation Letters*, vol. 8, no. 3, pp. 1351–1358, 2023, doi: 10.1109/LRA.2023.3239306.
- [70] J. Chen, J. Yan, Y. Qiu, H. Fang, J. Chen, and S. S. Cheng, “A cross-entropy motion planning framework for hybrid continuum robots,” *IEEE Robotics and Automation Letters*, vol. 8, no. 12, pp. 8200–8207, 2023, doi: 10.1109/LRA.2023.3325777.
- [71] P. J. Sincak *et al.*, “Sensing of continuum robots: A review,” *Sensors*, vol. 24, no. 4, p. 1311, 2024, doi: 10.3390/s24041311.
- [72] S. E. Navarro *et al.*, “A model-based sensor fusion approach for force and shape estimation in soft robotics,” *IEEE Robotics and Automation Letters*, vol. 5, no. 4, pp. 5621–5628, 2020, doi: 10.1109/LRA.2020.3008120.
- [73] F. Xu, H. Wang, W. Chen, and Y. Miao, “Visual servoing of a cable-driven soft robot manipulator with shape feature,” *IEEE Robotics and Automation Letters*, vol. 6, no. 3, pp. 4281–4288, 2021, doi: 10.1109/LRA.2021.3067285.
- [74] F. Campisano *et al.*, “Teleoperation and contact detection of a waterjet-actuated soft continuum manipulator for low-cost gastroscopy,” *IEEE Robotics and Automation Letters*, vol. 5, no. 4, pp. 6427–6434, 2020, doi: 10.1109/LRA.2020.3013900.
- [75] A. Pore *et al.*, “Autonomous navigation for robot-assisted intraluminal and endovascular procedures: A systematic review,” *IEEE Transactions on Robotics*, vol. 39, no. 4, pp. 2529–2548, 2023, doi: 10.1109/TRO.2023.3269384.
- [76] S. R. Ravigopal, T. A. Brumfiel, A. Sarma, and J. P. Desai, “Fluoroscopic image-based 3-d environment reconstruction and automated path planning for a robotically steerable guidewire,” *IEEE Robotics and Automation Letters*, vol. 7, no. 4, pp. 11918–11925, 2022, doi: 10.1109/LRA.2022.3207568.
- [77] I. Tamadon *et al.*, “Semiautonomous robotic manipulator for minimally invasive aortic valve replacement,” *IEEE Transactions on Robotics*, vol. 39, no. 6, pp. 4500–4519, 2023, doi: 10.1109/TRO.2023.3315966.
- [78] X. Huang, J. Zou, and G. Gu, “Kinematic modeling and control of variable curvature soft continuum robots,” *IEEE/ASME Transactions on Mechatronics*, vol. 26, no. 6, pp. 3175–3185, 2021, doi: 10.1109/TMECH.2021.3055339.
- [79] M. Zhao, F. Shi, T. Anzai, K. Okada, and M. Inaba, “Online motion planning for deforming maneuvering and manipulation by multilinked aerial robot based on differential kinematics,” *IEEE Robotics and Automation Letters*, vol. 5, no. 2, pp. 1602–1609, 2020, doi: 10.1109/LRA.2020.2967285.
- [80] H. Nigatu and D. Kim, “Optimization of 3-dof manipulators’ parasitic motion with the instantaneous restriction space-based analytic coupling relation,” *Applied Sciences*, vol. 11, no. 10, p. 4690, 2021, doi: 10.3390/app11104690.